The influence of galaxy environment on the stellar initial mass function of early-type galaxies

Rosani, Giulio; Pasquali, Anna; La Barbera, Francesco; Ferreras, Ignacio; Vazdekis, Alexandre

IMPORTANT NOTE: You are advised to consult the publisher's version (publisher's PDF) if you wish to cite from it. Please check the document version below.

Document Version
Publisher's PDF, also known as Version of record

Link to publication in University of Groningen/UMCG research database

The influence of galaxy environment on the stellar initial mass function of early-type galaxies

Giulio Rosani,[1,2]⋆ Anna Pasquali,[1] Francesco La Barbera,[3] Ignacio Ferreras[4] and Alexandre Vazdekis[5,6]

[1]*Astronomisches Rechen-Istitut, Zentrum für Astronomie, Universität Heidelberg, Mönchhofstr. 12-14, D-69120 Heidelberg, Germany*
[2]*Kapteyn Astronomical Institute, University of Groningen, PO Box 800, NL-9700AV Groningen, the Netherlands*
[3]*INAF – Osservatorio Astronomico di Capodimonte, Salita Moiariello 16, I-80020 Napoli, Italy*
[4]*Mullard Space Science Laboratory, University College London, Dorking, Surrey RH5 6NT, UK*
[5]*Instituto de Astrofísica de Canarias, E-38200 La Laguna, Tenerife, Spain*
[6]*Departamento de Astrofísica, Universidad de La Laguna, E-38205 La Laguna, Tenerife, Spain*

ABSTRACT

In this paper, we investigate whether the stellar initial mass function (IMF) of early-type galaxies depends on their host environment. To this purpose, we have selected a sample of early-type galaxies from the SPIDER catalogue, characterized their environment through the group catalogue of Wang et al., and used their optical Sloan Digital Sky Survey (SDSS) spectra to constrain the IMF slope, through the analysis of IMF-sensitive spectral indices. To reach a high enough signal-to-noise ratio, we have stacked spectra in velocity dispersion (σ_0) bins, on top of separating the sample by galaxy hierarchy and host halo mass, as proxies for galaxy environment. In order to constrain the IMF, we have compared observed line strengths and predictions of MIUSCAT/EMILES synthetic stellar population models, with varying age, metallicity, and 'bimodal' (low-mass tapered) IMF slope (Γ_b). Consistent with previous studies, we find that Γ_b increases with σ_0, becoming bottom-heavy (i.e. an excess of low-mass stars with respect to the Milky Way like IMF) at high σ_0. We find that this result is robust against the set of isochrones used in the stellar population models, as well as the way the effect of elemental abundance ratios is taken into account. We thus conclude that it is possible to use currently state-of-the-art stellar population models and intermediate resolution spectra to consistently probe IMF variations. For the first time, *we show that there is no dependence of Γ_b on environment or galaxy hierarchy, as measured within the 3 arcsec SDSS fibre, thus leaving the IMF as an intrinsic galaxy property, possibly set already at high redshift.*

Key words: galaxies: elliptical and lenticular, cD – galaxies: evolution – galaxies: fundamental parameters – galaxies: groups: general – galaxies: stellar content.

1 INTRODUCTION

The study of the formation and evolution of early-type galaxies (ETGs) has been carried out for a long time, yet today it still poses some interesting challenges. Today's increasingly accepted scenario for the formation of ETGs is the two-phase scenario (Mo, van den Bosch & White 2010; Oser et al. 2010; Naab 2013), in which roughly half the final mass of the galaxy is formed in a relatively short starburst phase at high redshift (the formation phase), followed by a second phase, where the other half is accreted over time through galaxy–galaxy interactions such as minor and major mergers (the assembly phase, see also De Lucia et al. 2006). The

properties of the stellar population, formed during the initial starburst, are found to correlate with the central velocity dispersion, hence with the mass, of the galaxy (Faber 1973; Worthey, Faber & Gonzalez 1992; Trager et al. 2000; Gallazzi et al. 2006; Graves, Faber & Schiavon 2009a,b; Kuntschner et al. 2010; McDermid et al. 2015, but see also Renzini 2006 and references therein), with more massive galaxies having higher [α/Fe], indicative of shorter and more intense starbursts, as well as older and more metal-rich stellar populations (Vazdekis et al. 1996, 1997; Thomas et al. 2005). Radial gradients of age, metallicity, and elemental abundances obtained by Greene et al. (2015) indicate that, while these populations dominate the ETGs central regions, the galaxy outskirts are made up of metal-poorer stars. Such metal-poor populations may have been accreted over time from smaller systems (La Barbera et al. 2012; Huang et al. 2016). Extended stellar features observed in many ETGs (see

⋆ E-mail: g.rosani@rug.nl

Duc et al. 2015) suggest, in fact, that galaxy interactions are common, and simulations show that in the event of a minor merger the stellar content of the less-massive galaxy undergoing the merger is deposited in the outskirts of the more massive stellar system. Major mergers on the other hand are capable of mixing the stellar content of both galaxies, but happen, in general, only once in the lifetime of an ETG (Bernardi 2009; Trujillo, Ferreras & de La Rosa 2011; Oser et al. 2012; Naab 2013).

An important factor, regulating the type and rate of mergers that galaxies may have undergone, is the environment where they reside. Following the approach used in semi-analytic models (SAMs) of galaxy formation and evolution, environment can be characterized by the mass of the dark matter (DM) host halo that galaxies are bound to. Moreover, these galaxies can be split between the host central galaxy, which is the most massive one, and satellites. Theoretical predictions as well as observations show the evolutionary paths of these two galaxy types to be rather different. Centrals are situated in a spot where the host halo enables them to accrete gaseous and stellar material from satellites, while satellites are being stripped of their stars and gas by tidal and ram-pressure stripping, respectively (Gunn & Gott 1972; Bekki 2009; Kapferer et al. 2009; Villalobos et al. 2012; Chang, Macciò & Kang 2013). In this way, the star formation (SF) of centrals is more extended in time, while the SF in satellites is quenched by environment, thus making galaxy hierarchy influence the overall stellar population properties of galaxies (Pasquali et al. 2009, 2010; Rogers et al. 2010; de La Rosa et al. 2011; La Barbera et al. 2014; Pasquali 2015).

Representing environment with the halo DM mass allows us to correlate galaxy properties with a global measurement of environment and to directly compare observational trends with what is predicted by SAMs. On the contrary, the projected number density of satellites, which is often used in the literature to quantify environment, does not allow such a direct comparison. For example, the projected number density of satellites in a small galaxy group most likely describes the whole environment, while it delivers only a measurement of the local environment in the case of galaxy clusters (Pasquali et al. 2009, 2010; Pasquali 2015).

Since galaxy environment has been shown to influence the stellar population content of galaxies, a fundamental question is to assess to what an extent different stellar population properties depend on hierarchy and the environment where galaxies reside. In this work, we focus on one of these properties, i.e. the stellar initial mass function (IMF) of ETGs.

In recent years, the stellar IMF of ETGs has been found to deviate significantly from the Galactic function, i.e. either a Kroupa (2001) or a Chabrier (2005) distribution, with growing evidence for an excess of low-mass stars, i.e. a bottom-heavy IMF, in more, relative to less, massive galaxies (Vazdekis et al. 1996, 1997, 2003; Cenarro et al. 2003; van Dokkum & Conroy 2010, 2011, 2012; Conroy & van Dokkum 2012a,b; Ferreras et al. 2013, 2015b; La Barbera et al. 2013; Spiniello et al. 2014; Ferreras, La Barbera & Vazdekis 2015a; La Barbera, Ferreras & Vazdekis 2015; Martín-Navarro et al. 2015c; Conroy, van Dokkum & Villaume 2017). Such evidence for a non-universal IMF has been confirmed with different observational methods:

Dynamics. The total, dynamical mass (or mass-to-light ratio, M/L) of an ETG is derived, and then the stellar mass (or $M_\star/L$) is inferred, based on some assumption on the underlying DM distribution, and compared to the expected value for a Kroupa-like IMF (Thomas et al. 2011b; Cappellari et al. 2012, 2013; Dutton, Mendel & Simard 2012; Wegner et al. 2012; Dutton et al. 2013; Tortora, Romanowsky & Napolitano 2013; McDermid et al. 2014; Davis & McDermid 2017).

Spectral analysis – IMF-sensitive features in the spectra of ETGs are compared to predictions of synthetic stellar population models with varying IMF, either through the analysis of line-strengths or spectral fitting, to constrain directly the fraction of low-mass stars in the IMF (Spinrad 1962; Cohen 1978; Faber & French 1980; Carter, Visvanathan & Pickles 1986; Hardy & Couture 1988; Delisle & Hardy 1992; Saglia et al. 2002; Cenarro et al. 2003; Falcón-Barroso et al. 2003; van Dokkum & Conroy 2010, 2011, 2012; Conroy & van Dokkum 2012a,b; Smith, Lucey & Carter 2012; Spiniello et al. 2012, 2014; Ferreras et al. 2013, 2015a,b; La Barbera et al. 2013, 2015; Martín-Navarro et al. 2015c; van Dokkum et al. 2017).

Lensing– The total mass projected within the Einstein radius is measured. Based on assumptions on the DM component, the stellar mass is inferred, and compared to expectations (based on photometry/spectroscopy) for a Kroupa-like IMF (Ferreras, Saha & Williams 2005; Ferreras, Saha & Burles 2008; Auger et al. 2010; Ferreras et al. 2010; Treu et al. 2010; Barnabè et al. 2011; Spiniello et al. 2015; Newman et al. 2016). This method differs from dynamics not only in the techniques used to constrain the total mass (or M/L), but also in that it constrains the 2D projection of the mass of the galaxy on the lens plane and not the 3D distribution of the mass as dynamical studies do.

While, in principle, spectroscopy allows the IMF shape to be directly constrained (Conroy & van Dokkum 2012a), lensing and dynamics do actually constrain only the IMF normalization (i.e. the stellar mass), which is affected by either low-mass stars (i.e. a bottom-heavy distribution) or stellar remnants (i.e. a top-heavy distribution, with an excess of giant, relative to dwarf, stars relative to the Milky Way distribution). Moreover, some works have found evidence for a Kroupa-like IMF normalization in some massive ETGs, leaving the debate on the IMF slope in ETGs open (see Smith & Lucey 2013; Smith, Lucey & Conroy 2015; Leier et al. 2016).

From a theoretical point of view, there is no commonly accepted framework to explain the origin of a non-universal, bottom-heavy, IMF in massive galaxies. Indeed, a top-heavy IMF has been invoked to explain the high [α/Fe] observed in massive ETGs, since the downsizing in SF alone is not able to reproduce the values of [α/Fe] observed (De Masi, Matteucci & Vincenzo 2018). Furthermore, the possibility of an IMF slope dependent on the instantaneous star formation rate (SFR) has been proposed by Gunawardhana et al. (2011) and Weidner et al. (2013), with the IMF becoming increasingly top-heavy with increasing SFR. This idea has also been tested in the GAEA SAMs (Fontanot et al. 2017; De Lucia, Fontanot & Hirschmann 2017), where an IMF changing with the instantaneous SFR has been found to reproduce the enhanced [α/Fe] of ETGs. In order to reconcile the high metal content and enhanced [α/Fe] of ETGs with a bottom-heavy IMF, a time-dependent scenario seems to be actually required, where the IMF switches from a top- to bottom-heavy phase during the initial phases of collapse (Vazdekis et al. 1997; Weidner et al. 2013; Ferreras et al. 2015b), perhaps due to the rapid injection of energy into a highly dense and turbulent interstellar medium (Hopkins 2013; see also Chabrier, Hennebelle & Charlot 2014). The mechanism(s) behind such variations of IMF slope with SFR and time are still unclear, though. In this regard, studying the dependence of IMF on environment might provide some further clue, as galaxies belonging to different environments

are expected to have experienced different physical conditions at their formation, as well as different SFHs during their evolution.

Last but not least, radial gradients in IMF slope have been recently found for a number of massive ETGs (Martín-Navarro et al. 2015a; La Barbera et al. 2016). The central regions of these objects show a bottom-heavy IMF, while the outskirts follow a Kroupa-like distribution (but see Alton, Smith & Lucey 2017). Interestingly, this feature could be explained in light of the two-phase formation scenario for massive ETGs described above.

In this work, we focus on the spectroscopic approach to constrain the IMF, measuring, for the first time, how the IMF changes with velocity dispersion in ETGs, as a function of hierarchy as well as the environment where galaxies reside. To this aim, we analyse a set of optical and NIR line-strengths in stacked spectra of ETGs from the Sloan Digital Sky Survey (SDSS), following a similar methodology as that adopted in our previous works (Ferreras et al. 2013; La Barbera et al. 2013, 2015). The layout of the paper is the following. In Sections 2 and 3, we present the data and models used in the analysis, respectively. Section 4 describes our methodology, while Section 5 and 6 present and discuss the results. Conclusions are drawn in Section 7.

2 DATA

The SPIDER[1] catalogue contains 39 993 galaxies in the redshift range $0.05 < z < 0.095$, classified as ETGs because of their passive spectra and bulge dominated morphology (following the definition of Bernardi et al. 2003). The bona-fide ETGs version of the catalogue, with better quality SDSS spectroscopy available (see La Barbera et al. 2013), also imposes that the galaxies meet the following criteria:

(i) central velocity dispersion $\sigma_0 \geq 100 \, \mathrm{km \, s^{-1}}$,
(ii) $E(B - V) < 0.1$ mag,
(iii) $\mathrm{S/N(Å^{-1})} > (14, 27, 21)$ for $\sigma_0 = (100, 200, 300) \, \mathrm{km \, s^{-1}}$,

which results in a reduced sample of $N_G = 24\,781$ SPIDER ETGs. Finally, a visual inspection of the morphology of these objects, aimed at removing late-type galaxies with a prominent bulge, reduces the sample to 21 665 ETGs.

We match the final SPIDER ETG sample with the 596 851 galaxies in the group catalogue by Wang et al. (2014), which is the version of the group catalogue of Yang et al. (2007) updated to SDSS DR7, and obtain a final sample of 20 996 SPIDER ETGs for which we have both environmental information from the group catalogue and a spectrum available from SDSS (DR12).

We correct the flux of the retrieved spectra for Galactic extinction, using the Schlegel maps (Schlafly & Finkbeiner 2011) obtained from the IRSA website[2] and by adopting the Galactic extinction law by Cardelli, Clayton & Mathis (1989). We also correct the spectra for redshift and transform them from the vacuum system to the air system, following Morton (1991), in order to later compare them with MIUSCAT/EMILES synthetic stellar population models (see Section 3). To this effect, the spectra were interpolated with a linear spline into a common wavelength grid, spanning the range 3800–8800 Å, with a fixed dispersion of 1 Å. We chose the wavelength range to be in common to most of the spectra, at the same time including all the (optical and NIR) absorption features

required for the analysis (see La Barbera et al. 2013 for details). Finally, we redefined the uncertainty on the flux by reinterpolating the spectrum, offset by $\pm 1\sigma_{\mathrm{flux}}$, respectively, and then by taking the halved difference between the two interpolated spectra as the new uncertainty.

2.1 Environment

The Wang et al. (2014) and the Yang et al. (2007) catalogues use an iterative routine to find galaxy groups and assign a galaxy to a given group, which is represented by its DM host halo mass. The routine first uses an Friends-of-Friends algorithm with small linking lengths in redshift space to tentatively assign galaxies to groups and estimate the group's total stellar mass through its total luminosity. It then uses an iterative procedure to assign a mass to the DM host halo of the group based on the average M/L of the groups found in the previous iteration. With a mass assigned to the host halo, the routine estimates the size and velocity dispersion of the group and reassigns the membership. This part is repeated until convergence to a final result is reached. The routine also labels the most massive galaxy in the group as the central, while all the other galaxies assigned to the group are considered satellites. The calculation of the stellar mass of the galaxies is performed using the relation of Bell et al. (2003) between stellar M/L and colour. The DM masses, on the other hand, have been obtained using both the total characteristic luminosity and stellar mass of the groups (see Yang et al. 2007 for more details).

Hence, for each SPIDER ETG, the information we extract from the Wang et al. (2014) catalogue is the DM halo mass of its parent group, as derived from the group total stellar mass,[3] and the hierarchy of the galaxy itself (satellite or central). We first split the galaxy sample into two subsamples, based on galaxy hierarchy: subsample CEN for the centrals (15 571 objects), and subsample SAT for the satellites (5425 objects). This first subdivision is made regardless of the mass of the host halo the galaxies reside in and allows us to see if galaxy hierarchy influences the properties derived from the spectra, i.e. age, metallicity, [α/Fe], and, in particular, the IMF slope (Γ_b).

In addition, we created two subsamples for each hierachical subsample by differentiating between galaxies inhabiting high- and low-mass host haloes. The cut in host halo mass was set to $10^{12.5}$ and $10^{14} \, \mathrm{M_\odot} \, h^{-1}$ for centrals and satellites, respectively, resulting in the following subsamples:

(i) C1 ($M_h < 10^{12.5} \, \mathrm{M_\odot} \, h^{-1}$) with $N_{\mathrm{ETGs}} = 10515$;
(ii) C2 ($M_h \geq 10^{12.5} \, \mathrm{M_\odot} \, h^{-1}$) with $N_{\mathrm{ETGs}} = 5027$;
(iii) S1 ($M_h < 10^{14} \, \mathrm{M_\odot} \, h^{-1}$) with $N_{\mathrm{ETGs}} = 3284$;
(iv) S2 ($M_h \geq 10^{14} \, \mathrm{M_\odot} \, h^{-1}$) with $N_{\mathrm{ETGs}} = 2093$.

This division closely follows the one made in La Barbera et al. (2014), hereafter LB14, with the only difference being that the satellite subsample is not further subdivided with respect to their group-centric distance. The difference in the mass cut is justified by the distribution of host halo mass for centrals and satellites, as seen in Fig. 1 (top right-hand panel). Furthermore, the cut at $M_h = 10^{12.5} \, \mathrm{M_\odot} \, h^{-1}$ for centrals is compatible with a halo hosting an L^* galaxy (Moster et al. 2010).

Fig. 1 shows the distribution of four properties of our galaxy sample for both the CEN and the SAT subsamples. We see that the

---

[1] Spheroids Panchromatic Investigation in Different Environmental Regions, La Barbera et al. (2010).
[2] http://irsa.ipac.caltech.edu/applications/DUST/

[3] As shown in More et al. (2011), the total stellar mass is a better proxy of the halo mass compared to total luminosity.
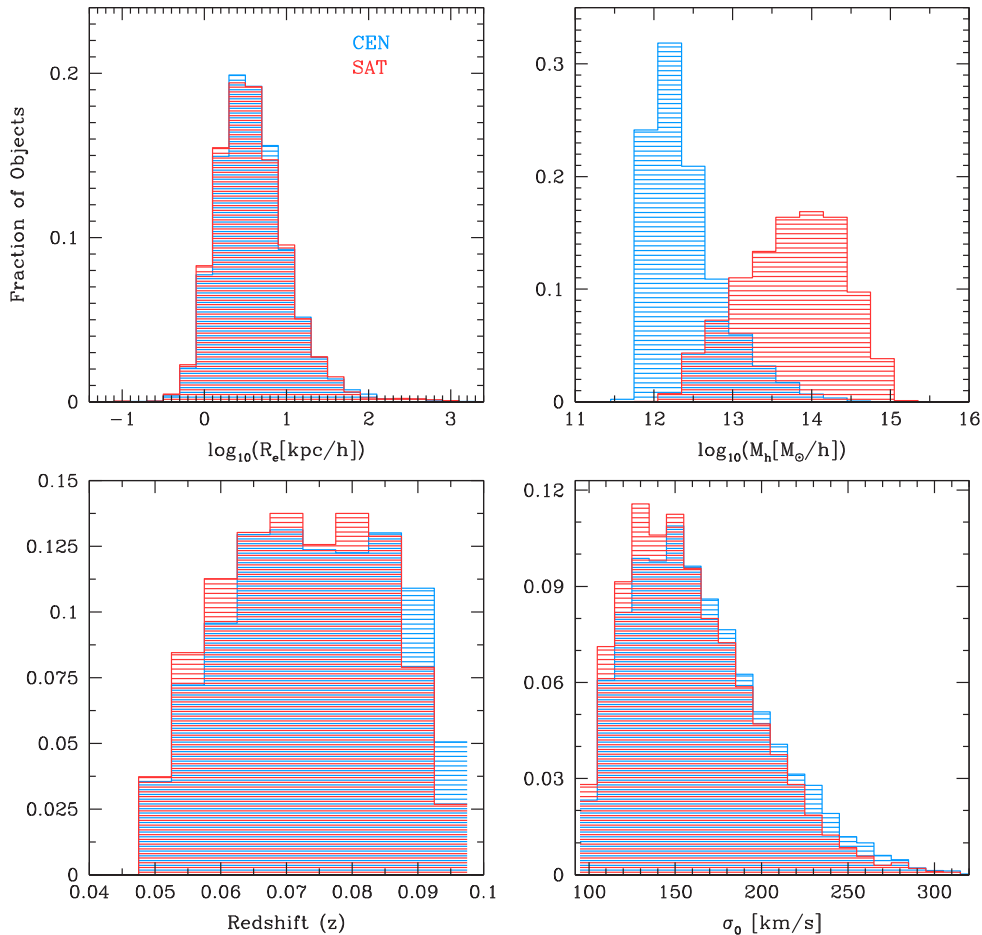
Figure 1. Distribution of various properties for centrals (in blue) and satellites (in red). The upper two panels show, respectively, the distribution of the sample galaxies in effective radius (left-hand panel) and host halo mass (right-hand panel), whereas the lower two panels show the distribution in redshift (left-hand panel) and central velocity dispersion (right-hand panel). There is only a distinction in distribution between centrals and satellites when they are binned in host halo mass.

histograms of centrals and satellites are very similar, except for their distribution in host halo mass. This is not surprising, since lower mass haloes are believed to be more frequent in the Universe and since centrals follow the host halo distribution closely. On the other hand, the distribution of satellites results from the fact that these galaxies are more numerous in more massive host haloes, but at the same time such haloes are rare in the Universe. Hence, following LB14, we adopt two different host halo mass cuts for centrals and satellites, based on the peaks of the CEN and SAT distributions. Finally, we notice that the number of objects given above for subsamples C1/C2 and S1/S2 does not sum to the number of objects given for CEN and SAT, because the subsamples C1/C2 and S1/S2 are counted after the bins in central velocity dispersion have been constructed, and some galaxies have been rejected accordingly (see Section 2.2 for details). After such binning, the CEN and SAT subsamples are reduced to 15 559 and 5408 objects, respectively.

2.2 Stacked spectra

To measure the effect of the IMF on absorption features, we need high signal-to-noise ratio spectroscopy (S/N $\gtrsim$ 100 Å^{-1}; see e.g. Conroy & van Dokkum 2012a). To this aim, we stack the spectra of ETGs in central velocity dispersion (σ_0) bins, following a similar procedure as in La Barbera et al. (2013), hereafter LB13 and LB14.

The σ_0-bins span the range [100,310] km s^{-1} and are generally 10 km s^{-1} wide. They are defined so as to contain at least 40 objects each, and, should this not be the case, they are widened by 10 km s^{-1} until a maximum width of 30 km s^{-1} is reached. If the condition is still not met, the bin is rejected. The stacking procedure allows us to raise the quality of the spectra, but at the cost of obtaining an average behaved spectrum over the galaxy population in the bin.

For each bin, in order to account for differences in the absorption features due to the galaxies' kinematics, we broaden the spectra to the upper value of σ_0 in the bin, by convolving the spectra with an appropriate Gaussian function. We then proceed to stack the spectra, by first normalizing each of them by its median flux in the wavelength range [5000–8000] Å. Once this is done for all the spectra in the bin, we multiply all normalized spectra by the median flux of the median fluxes found for each individual spectrum. This puts all the spectra in one bin at roughly the same flux level and allows differences in flux to be exclusively due to noise.

We compute the stacked spectrum by taking the median flux, at each wavelength, of all the processed spectra in the σ_0 bin. The resulting stacks have an enhanced S/N, by a factor of at least ~10, with respect to the single spectra in each bin.

Fig. 2 shows the median S/N ratio of the stacked spectra – measured per Å in the region [4840–4880] Å – as a function of σ_0, for our different galaxy subsamples. All stacks have an S/N above 100.
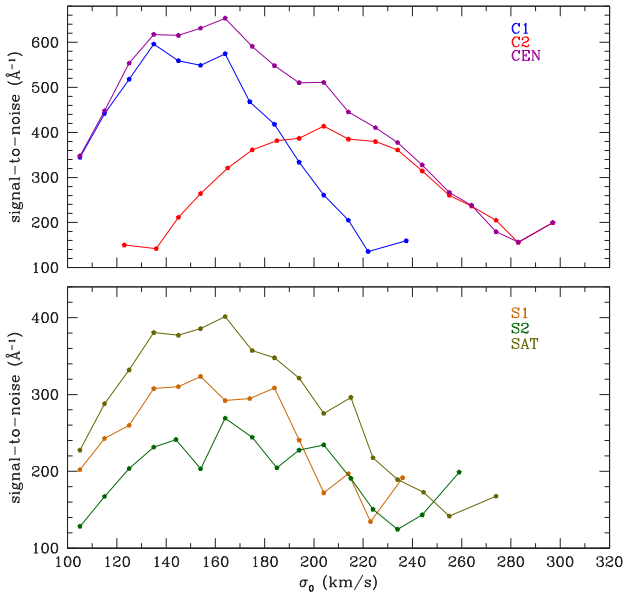
Figure 2. S/N ratio of the stacked spectra analysed in this work, as a function of σ_0. The upper and lower panels refer to the different subsamples of central and satellite ETGs, respectively.

During the procedure, the resolution of the spectra remained that of SDSS, while the dispersion was fixed at $1\,\text{Å}\,\text{pix}^{-1}$ for the whole wavelength range.

3 SYNTHETIC STELLAR POPULATION MODELS

For each stacked spectrum, we measure the line strengths for a given set of spectral indices and compare them to those predicted from synthetic stellar population models. The models used in this work are the MIUSCAT models of Vazdekis et al. (2012), and the EMILES models of Vazdekis et al. (2016).

The MIUSCAT models cover the wavelength range [3465–9469] Å and are constructed using the MILES (Sánchez-Blázquez et al. 2006), CaT (Cenarro et al. 2001), and Indo-U.S. (Valdes et al. 2004) empirical stellar libraries. These libraries cover the wavelength range [3525–7500], [8350–9020], and [3465–9469] Å, respectively. The Indo-U.S. is only used to fill the gap between the MILES and CaT spectral libraries. MIUSCAT models are computed at a fixed spectral resolution of 2.51 Å (full width at half-maximum).

EMILES models extend MIUSCAT both bluewards and redwards, to 1680.2 Å and ~5 μm, respectively. These models are constructed using spectra from the IRTF[4] stellar library (Cushing, Rayner & Vacca 2005; Rayner, Cushing & Vacca 2009) to extend the MIUSCAT models towards the infrared (Röck et al. 2016), and using spectra from the NGSL[5] spectral library (Gregg et al. 2006; Koleva & Vazdekis 2012) to extend MIUSCAT bluewards.

Both MIUSCAT and EMILES SSPs are computed for several IMFs, including unimodal (single power law) and bimodal (low-mass tapered) IMFs, both characterized by their slope, Γ (unimodal), and Γ_b (bimodal) as a single free parameter (see e.g. Vazdekis et al. 1996, 2003; Ferreras et al. 2015b). The bimodal IMFs are given by a power-law smoothly tapered off below a characteristic 'turnover' mass of $0.6\,\text{M}_\odot$. For $\Gamma_b \sim 1.3$, the bimodal IMF

---

[4] Infrared Telescope Facility.
[5] Next Generation Spectral Library.

gives a good representation of the Kroupa IMF, while for $\Gamma \sim 1.35$ the unimodal IMF coincides with the Salpeter (1955) distribution. The lower and upper mass cut-offs of the IMFs are set to 0.1 and $100\,\text{M}_\odot$, respectively. Since the bimodal distribution consists of a power law at the high-mass end, while it is smoothly tapered towards low masses, varying Γ_b changes the dwarf-to-giant ratio in the IMF through the normalization. While this approach is different with respect to a change of the IMF slopes at low mass and very low mass (e.g. Conroy & van Dokkum 2012b), this parametrization is good enough for our purposes, as in this work we do not aim at constraining the IMF shape in detail, but rather to study the possible dependence of IMF variations on galaxy environment. In addition, the bimodal IMF has been found to provide a consistent explanation between optical and NIR IMF-sensitive features, and consistent constraints to dynamical models, in contrast to the unimodal distribution (La Barbera et al. 2016; Lyubenova et al. 2016).

Since the wavelength range of our stacked spectra is fully covered by MIUSCAT/EMILES models, for the purpose of our analysis, the only difference between the two sets of models is the range of IMF slope for which they are computed. EMILES reaches a higher maximum value of $\Gamma_b = 3.5$ (instead of 3.3, for MIUSCAT), with a better sampling of the range $2.0 < \Gamma_b < 3.0$, and thus we compare the stacked spectra to EMILES models in our final results.

Both MIUSCAT and EMILES models have been generated using the isochrones of Girardi et al. (2000), hereafter called Padova isochrones. In addition to the Padova isochrones, we also generated EMILES models using the isochrones of Pietrinferni et al. (2004) and Pietrinferni et al. (2006), hereafter Teramo isochrones. The MIUSCAT and EMILES Teramo models were used to test the robustness of our results against the ingredients of stellar population models.

Table 1 summarizes the values of Γ_b, metallicity, and age used to construct the models. Different sets of isochrones have different values of age and metallicity, with a different sampling. While the Padova isochrones sample their age range logarithmically with smaller steps for younger ages with respect to older ages, the Teramo isochrones sample the age range linearly with a step that varies based on the age of the stellar population (see Vazdekis et al. 2015 for details). In Section 5.4, we compare results obtained for different models.

4 ANALYSIS OF LINE STRENGTHS

In order to constrain galaxy age, metallicity, [α/Fe], and IMF slope, for each stacked spectrum we measure the equivalent widths of a set of specific line indices. The age parameter is mainly constrained through Hβ_o, the optimized Hβ index defined by Cervantes & Vazdekis (2009). To this effect, we correct the index for nebular emission contamination with a similar procedure as that described in LB13, i.e. estimating the excess of flux in the line with respect to a combination of two MIUSCAT SSPs that best fit the Hβ spectral region ($\lambda\lambda = 4530$–4730 Å) when excluding the trough of the absorption. For each stack, the emission correction is determined separately for models with different Γ_b, and then applied iteratively when the IMF slope is being determined (see below). Metallicity is mainly constrained through the total metallicity indicator [MgFe]$'$ (Thomas, Maraston & Bender 2003), which is insensitive to [α/Fe].

Table 2 shows the set of line indices used in the fits (the two different cases, '.0' and '.1', will be explained in Subsection 4.1) and the expected sensitivity of each index to different stellar population properties. We also report the references where the central passband

Table 1. The table shows the IMF slopes, metallicities, and ages used to create the synthetic spectra of the three sets of simple stellar population models used in our analysis.

Model	Bimodal IMF slope (Γ_b)	Metallicity [Z/H]	Age (Gyr)
MIUSCAT (Padova00)	0.30, 0.80, 1.00, 1.30, 1.50, 1.80, 2.00, 2.30, 2.80, 3.30	−1.71, −1.31, −0.71, −0.40, +0.00, +0.22, +0.40	0.063 – 17.7828
EMILES (Padova00)	0.30, 0.50, 0.80, 1.00, 1.30, 1.50, 1.80, 2.00, 2.30, 2.50, 2.80, 3.00, 3.30, 3.50	−2.32, −1.71, −1.31, −0.71, −0.40, +0.00, +0.22	0.0631 – 17.7828
EMILES (Teramo)	0.30, 0.50, 0.80, 1.00, 1.30, 1.50, 1.80, 2.00, 2.30, 2.50, 2.80, 3.00, 3.30, 3.50	−2.27, −1.79, −1.49, −1.26, −0.96, −0.66, −0.35, −0.25 +0.06, +0.15, +0.26, +0.40	0.0300 – 14.0000

Table 2. Different sets of line indices used in the '.0' and '.1' methods to fit the observed line-strengths of stacked spectra to the ones obtained from SSP models (see text) when determining the IMF. The upper table also shows which abundances are fitted in the '.1' case and is analogous to the table in La Barbera et al. (2015), where a similar approach has been adopted. The lower part of the table shows how different line indices are defined and have been used in the fits, i.e. if they constrain the IMF, one or more of the given abundance ratios, age, metallicity, and [Mg/Fe]. References, reporting where the feature and pseudo-continuum bands of each index are defined, are listed in the last column of the lower table.

Method	Lines used		Abundances
'.0'	H β_o, [MgFe]′, TiO1, TiO2$_{SDSS}$, Mg4780, NaI8190, Ca2, CaH&K, NaD		None
'.1'	H β_o, [MgFe]′, TiO1, TiO2$_{SDSS}$, Mg4780, NaI8190, Ca2, CaH&K, NaD, Ca1, Ca4227, Fe4531, Mg1, Mg2, C4668, CN2, Mgb5177		[Ca/Fe], [Na/Fe], [Ti/Fe], [O/Fe], [C/Fe], [N/Fe], [Mg/Fe], [Si/Fe]

Index	IMF sensitive	Abundance fit	Other constraint	Definition
CaH&K	Yes	[Ca/Fe]	/	Serven, Worthey & Briley (2005)
CN2	No	[C/Fe], [N/Fe], [O/Fe]	/	Trager et al. (1998)
Ca4227	No	[Ca/Fe]	/	Trager et al. (1998)
Fe4531	No	[Ti/Fe]	/	Trager et al. (1998)
C4668	No	[C/Fe]	/	Trager et al. (1998)
Mg4780	Yes	No	/	Serven et al. (2005)
H β_o	No	No	Age indicator	Cervantes & Vazdekis (2009)
Mg1	No	[C/Fe], [O/Fe], [Si/Fe]	/	Trager et al. (1998)
Mg2	No	[Mg/Fe], [Si/Fe]	/	Trager et al. (1998)
Mgb5177	No	[Mg/Fe]	[α/Fe] proxy	Trager et al. (1998)
[MgFe]′	No	No	Z-metallicity indicator	Thomas et al. (2003)
Fe3	No	No	[α/Fe] proxy	Kuntschner (2000)
NaD	Yes	[Na/Fe]	/	Trager et al. (1998)
TiO1	Yes	[Ti/Fe]	/	Trager et al. (1998)
TiO2$_{SDSS}$	Yes	[Ti/Fe]	/	La Barbera et al. (2013)
NaI8190	Yes	[Na/Fe]	/	La Barbera et al. (2013)
Ca1	No	[Ca/Fe]	/	Cenarro et al. (2001)
Ca2	Yes	No	/	Cenarro et al. (2001)

and pseudo-continuum bands of the lines have been defined. Additionally, Appendix A shows the trend of all spectral indices, for all stacked spectra, as a function of central velocity dispersion σ_0.

4.1 Fitting the measured indices

We compare observed line-strengths to a grid of predictions for SSP models with varying age, metallicity, and IMF slope. The grids are constructed by linearly interpolating the models performing 200 and 150 steps in age and metallicity, respectively. For each stacked spectrum, model line-strengths are computed by first smoothing both MIUSCAT and EMILES SSPs to match the σ_0 of the given stack. We also take the effect of instrumental resolution into account and its dependence on wavelength when smoothing the models to match the observed spectra. We consider two fitting approaches, indicated as '.0' and '.1', respectively.

In the case '.0', we adopt an approach very similar to that of LB13. We fit H β_o and [MgFe]′ (to constrain age and metallicity), plus a number of IMF-sensitive features, i.e. NaI8190, Ca2, [6] TiO1, TiO2$_{SDSS}$, and Mg4780, as well as NaD and CaH&K (which have some sensitivity to IMF, as well as to abundance ratios). We do *not* fit individual abundance ratios, but compare directly observed

[6] The main difference with respect to LB13 is that we do not consider the combined calcium-triplet index (CaT) in the present analysis, but only the Ca2. The reason for this choice is that the third CaT line, Ca3, is at the border of the SDSS spectral range, where the low quality of the spectra is not sufficient for our purposes, when binning spectra as function of both σ_0 (as in LB13) and environment/hierarchy. For the same reason, we include only Ca1 and Ca2 in the '.1' fitting approach (see below). Ca1 is excluded from the '.0' case, because it is more sensitive to [Ca/Fe] than IMF variations if compared to Ca2.

and model line-strengths. Since we rely on MIUSCAT/EMILES models, the abundance patterns, [X/Fe] (where X denotes a generic element), of the models follow closely those of stars in the disc of our Galaxy, i.e. they are approximately solar-scaled at solar and super-solar metallicity. On the contrary, massive ETGs have non-solar abundance ratios (Peletier 1989; Worthey et al. 1992; Weiss, Peletier & Matteucci 1995, but see also Renzini 2006 and references therein). To take this into account, we first correct all observed line-strengths to solar scale, following the method in LB13. In practice, we estimate [Mg/Fe] (independently of the '.0' case) for each stacked spectrum, by fitting the Mgb5177 and Fe3 indices, at fixed age (estimated through the Hβ_o–[MgFe]' diagram), with models that have a varying metallicity at fixed IMF slope.[7] The fits provide two metallicity estimates, [Z/H]$_{\rm Mg}$ and [Z/H]$_{\rm Fe}$, respectively. We derive [Mg/Fe] from the following ansatz:

$$[{\rm Mg/Fe}] = 0.55[Z_{\rm Mg}/Z_{\rm Fe}] \\ = 0.55([{\rm Z/H}]_{\rm Mg} - [{\rm Z/H}]_{\rm Fe}), \quad (1)$$

where the coefficient 0.55 has been determined in LB13, based on model predictions from Thomas, Maraston & Johansson (2011a) (see also Vazdekis et al. 2015). The estimate of [Mg/Fe] is then used to correct observed line-strengths to solar-scale (see LB13 for details).

The '.0' fitting procedure is performed by minimizing the χ^2:

$$\chi^2(\Gamma_{\rm b}) = \sum_{\rm indices} \frac{(I_{\rm measured}^{\rm corr} - I_{\rm mod})^2}{\sigma_I^2 + s_I^2}, \quad (2)$$

where $I_{\rm measured}^{\rm corr}$ are the equivalent widths of the stacked spectra, corrected to solar scale; $I_{\rm mod}$ are the model line-strengths; σ_I and s_I are the uncertainties on the measured line-strengths, and on the correction for non-solar abundance pattern, respectively. For Hβ_o, the correction for nebular emission is also applied iteratively.[8] The parameters fitted in the '.0' case are age, metallicity, and the IMF slope $\Gamma_{\rm b}$.

In the second fitting approach, named '.1', the $I_{\rm mod}$ terms in equation (2) are redefined as $I_{\rm mod.1} = I_{\rm mod} + \delta_X[{\rm X/Fe}]$, where $\delta_X = \delta(I)/\delta([{\rm X/Fe}])$ is the sensitivity of a given index I to a variation in the abundance pattern of element X. The coefficients δ_X are computed with the aid of Conroy & van Dokkum (2012a) stellar population models (CvD12 models), having a Chabriér IMF, old age (12.5 Gyr), and solar metallicity. The [X/Fe] abundance ratios are treated as free fitting parameters, together with IMF slope, age, and (total) metallicity. In order to constrain [X/Fe] properly, we enlarge the set of targeted spectral features with respect to case '.0', including also indices that are sensitive to individual abundance ratios. The list of indices used in both fitting approaches is summarized in Table 2. Comparing the results of cases '.0' and '.1', we test the robustness of our results, and investigate if and how much they are affected by possible degeneracies between IMF and abundance ratios. For case '.1', the fits do also provide abundance ratio estimates for our stacked spectra. However, studying the dependence of [X/Fe] on σ_0, environment, and hierarchy, is beyond the scope of this paper, and will be eventually presented in a forthcoming work.

---

[7] We adopt an IMF slope of $\Gamma_{\rm b}$=1.3, although the estimate of [Mg/Fe] does not depend significantly on $\Gamma_{\rm b}$, as shown in La Barbera et al. (2017).

[8] In practice, we start by applying the emission correction obtained with models having a Kroupa-like IMF. Then, once the IMF slope is derived, we apply the emission correction computed for that IMF, and repeat the whole fitting procedure. In general, the second estimate of IMF slope is very similar to that obtained in the first step, without any need of a further iteration.
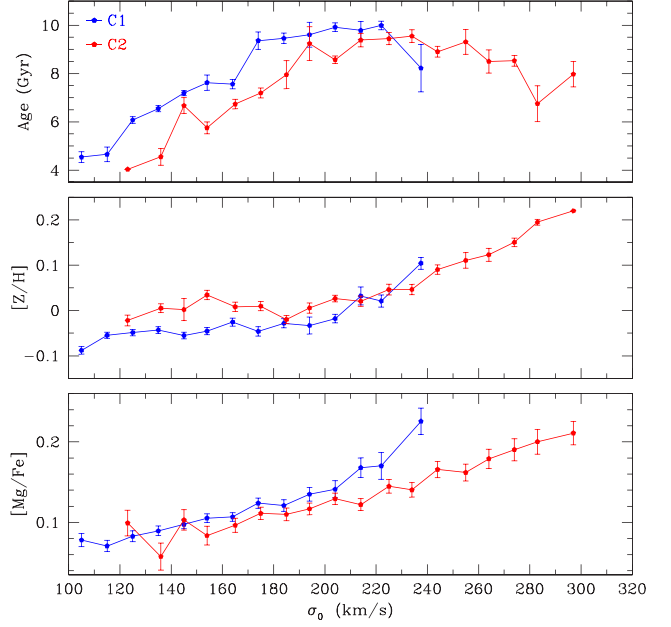

Figure 3. Trend of age, metallicity, and [Mg/Fe] with σ_0 for centrals in low- and high-mass haloes (subsamples C1 and C2), respectively. Age and metallicity are estimated through method '.0', while [Mg/Fe] is obtained from the '.1' fitting approach (see the text for details). C2 ETGs exhibit younger ages, higher metallicity and lower [Mg/Fe], than those in the C1 subsample, in agreement with La Barbera et al. (2014).

5 RESULTS

We present a comparison of age, metallicity, [Mg/Fe], and IMF slope for the different subsamples of centrals (Section 5.1), satellites (Section 5.2), and finally as a function of galaxy hierarchy (Section 5.3). We base our main results on EMILES Padova models, as different models (i.e. MIUSCAT versus EMILES; as well as different sets of isochrones) and different assumption on SFHs (2SSP versus1SSP) give very consistent results, as shown in Section 5.4.

5.1 Comparing centrals

Fig. 3 compares age, metallicity, and [Mg/Fe] – which is a proxy of [α/Fe] – for our subsamples of centrals, residing in low- (C1) and high- (C2) mass haloes, respectively. We consider metallicity and age estimates from method '.0' only. The reason for this choice is the following. In method '.1', we also include abundance ratios in the fitting procedure, computing the sensitivity of different indices to elemental abundances with CvD12 models (see above). Such models are computed at fixed [Fe/H], rather than total, metallicity (i.e. MIUSCAT/EMILES). Therefore, we consider the metallicity estimate from method '.1' less reliable than that from method '.0'. For [Mg/Fe], instead, we consider results from method '.1', as [Mg/Fe] is not fitted in the '.0' case. Notice that this approach is different from that of LB14, where we used the solar-scale proxy for [Mg/Fe] (see equation 1) and age/metallicity estimates inferred from the Hβ_o–[MgFe]' diagram. Our current results are very similar to those of LB14, though, as shown below.

We see that C2 centrals in high-mass haloes are generally slightly younger and metal richer (at $\sigma_0 \lesssim 220\,{\rm km\,s^{-1}}$) and have a slightly lower [Mg/Fe] with respect to C1 centrals in low-mass host haloes. We find an average difference of ΔAge = 1.2 Gyr, Δ[Z/H] = 0.041 dex, and Δ[Mg/Fe] = 0.03 dex, corresponding
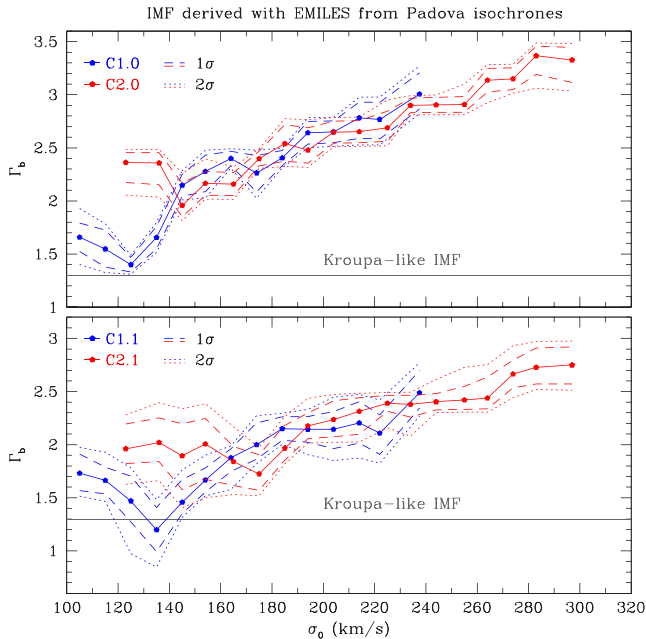
Figure 4. IMF slope, estimated through EMILES models with Padova isochrones (Vazdekis et al. 2016), for different subsamples of central ETGs. The upper panel shows the results of fitting only IMF sensitive indices (plus H β_o and [MgFe]′; i.e. the case '.0'), while the lower panel shows the results obtained when abundance ratios are also fitted (case '.1'). The dashed and dotted lines represent the 1σ and 2σ contours, respectively. We see no influence of environment on IMF slope for centrals, except for the two lowest bins of σ_0, where C2 ETGs have systematically higher Γ_b. This issue is further investigated in Section 6.3.1.

to a significance level of $\sim4\sigma$, $\sim2.6\sigma$, and $\sim1.7\sigma$ respectively. The metallicity and the [Mg/Fe] ratio rise with increasing σ_0, while the age first rises and then flattens around $\sigma_0 = 200\,\mathrm{km\,s^{-1}}$.

Fig. 3 is directly comparable to fig. 3 of LB14, where similar trends of age, metallicity, and [Mg/Fe] with σ_0 and halo mass are shown. We notice, however, that given the difference in methods used to derive these properties, our values of [Z/H] and [Mg/Fe] have an offset with respect to LB14 of $+0.1$ and -0.05 dex, respectively. Furthermore, the derived ages are lower by about 2 Gyr for the lowest and highest σ_0 bins.

The IMF slopes of subsamples C1 and C2, for both the '.0' and '.1' cases, are shown in Fig. 4. We see that the value of Γ_b also rises with increasing σ_0, turning the IMF from a Kroupa-like function ($\Gamma_b\sim1.3$) to a bottom-heavy distribution ($\Gamma_b\gtrsim 2.5$) at high central velocity dispersion. We do not observe a trend with host halo mass in the comparison of these two subsamples, but we notice that, for the lowest values of σ_0, C1 and C2 significantly differ in IMF slope. This issue is further investigated and discussed in Section 6.3.1.

5.2 Comparing satellites

Fig. 5 shows the comparison of age, metallicity, and [Mg/Fe] for our satellite subsamples, S1 and S2, respectively. All galaxy properties show the same behaviour with σ_0 as for the central subsamples (C1 and C2), with age, metallicity, and [Mg/Fe] all increasing with galaxy velocity dispersion. Differently from centrals, the trend of age with σ_0 for satellites does not depend significantly on environment (i.e. host halo mass), within the corresponding uncertainties (i.e. the average age difference is significant only at the $\sim1.3\sigma$ level). The same can be said for the differences in metallicity and [Mg/Fe],

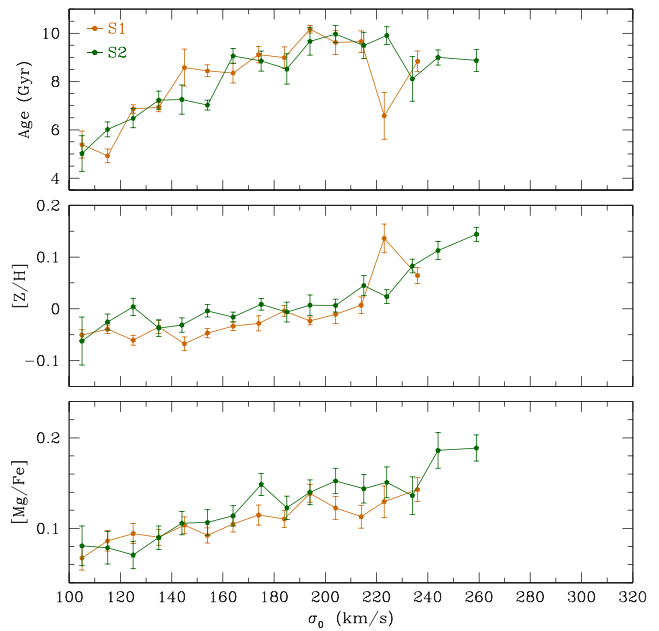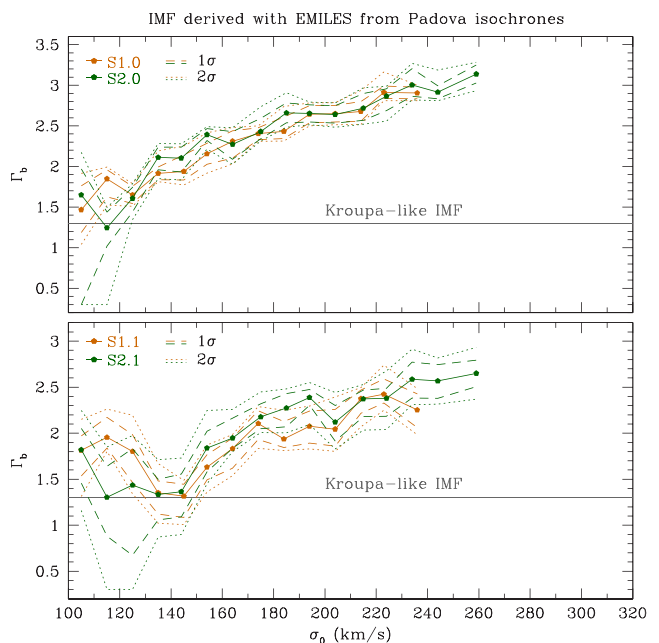**Figure 5.** Same as Fig. 3, but for the S1 and S2 subsamples.

Figure 6. Same as Fig. 4, but for the satellite subsamples. We see no influence of the environment on the IMF slope versus σ_0 trend, even for the lowest σ_0-bins.

which are only significant at $\sim1.5\sigma$ and 0.8σ, respectively. We conclude that environment does not influence the average properties of our satellite subsample, to our current precision.

Fig. 5 is qualitatively comparable to fig. 4 of LB14, where similar trends of age, metallicity, and [Mg/Fe] with σ_0 are found. The properties of satellites are shown to be independent of halo mass also in LB14.

The trend of IMF slope with σ_0 is very similar to that for central ETGs, as shown in Fig. 6. The IMF becomes increasingly bottom-heavier for higher σ_0 and no trend with host halo mass is observed, within the error bars.
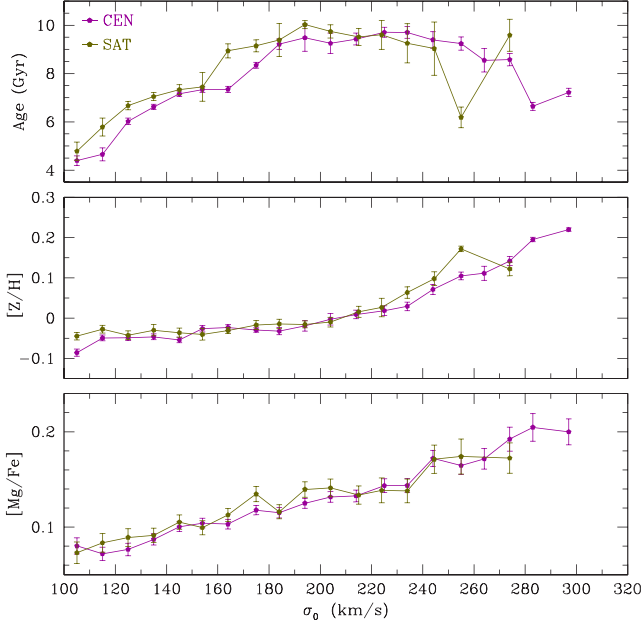
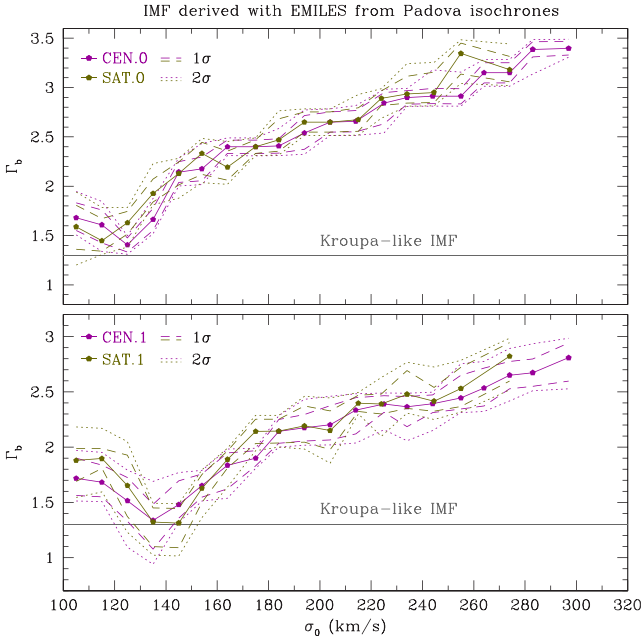**Figure 7.** Same as Figs 3 and 5, but comparing galaxies according to hierarchy, i.e. centrals versus satellites.

Figure 8. Same as Figs 4 and 6, but for the CEN and SAT subsamples.

5.3 Centrals and satellites

Comparing centrals and satellites regardless of host halo mass yields the results shown in Fig. 7, for age, metallicity, and [Mg/Fe], and Fig. 8, for IMF slope.

In general, centrals show younger ages (ΔAge = 0.7 Gyr), slightly more metal-poor populations (Δ[Z/H] = 0.019 dex), and slightly lower values of [Mg/Fe] (Δ[Mg/Fe] = 0.01 dex) than satellites. The difference between these two subsamples is not as pronounced as when we compare centrals in different host haloes, with the age being, in fact, the only property whose differences are significant at a 1.8σ level on average. Differences in metal-
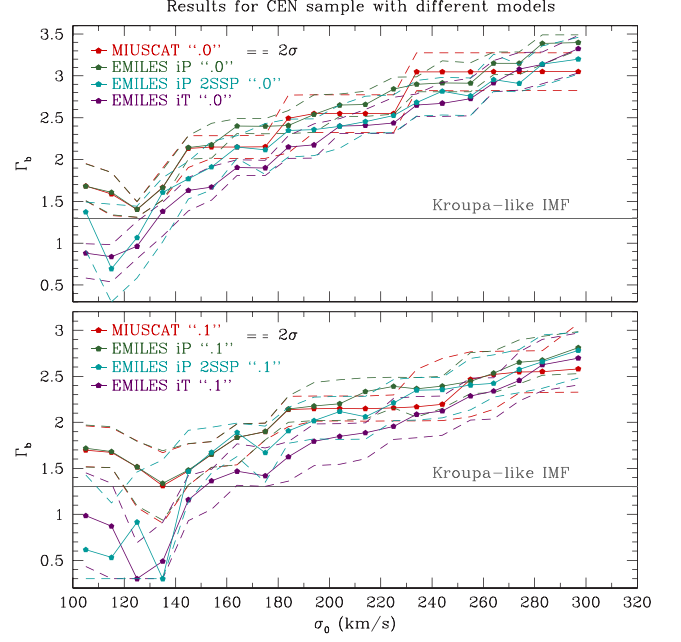
Figure 9. Comparison of IMF-slope estimates obtained using different models (see labels in the top left-hand of each panel), for the CEN subsample. The top and bottom panels refer to the cases '.0' and '.1', respectively. 'iP' refers to models based on Padova isochrones, while 'iT' refers to models based on Teramo isochrones. All curves refer to 1SSP models, but the cyan lines, which have been obtained for 2SSP models (see the text). To allow a more clear comparison of different curves, the plots show only the 2σ confidence contours on Γ_b.

licity and [Mg/Fe] can be considered not significant, since they differ only at a ~1.5σ and 0.7σ level, respectively. The behaviour of age, metallicity, and [Mg/Fe] with central velocity dispersion mirrors that already seen for the individual subsamples of centrals and satellites.

Fig. 8 shows that the IMF slope for the CEN and SAT subsamples behaves in the same way as for subsamples C1/C2 and S1/S2. At higher σ_0, the IMF becomes increasingly more bottom-heavy, while hierarchy does not affect the values of Γ_b significantly. We also reduced the range of halo mass for the central and satellite subsamples to $10^{12.5} \leq M_h < 10^{14} \, M_\odot \, h^{-1}$ to further check the robustness of our results. This test is equivalent to comparing the C2 and S1 subsamples and allows us to single out the effect of hierarchy (with respect to halo mass) on the IMF slope. We report no significant change in this comparison with respect to what shown in Fig. 8.

5.4 Comparison of results from different models

We repeat the fitting procedure for all stacked spectra, with different sets of models. In addition to MIUSCAT and EMILES single SSP (1SSP) models constructed with Padova isochrones (hereafter EMILES iP), we also perform the fits with EMILES models based on Teramo isochrones (EMILES iT), and EMILES iP models where, instead of using a single SSP, we adopt a linear combination of two SSPs (EMILES iP 2SSP), each having different age and metallicity (treated as free fitting parameters), and the same IMF.

Results obtained with different models are compared in Figs 9 and 10, for the CEN and SAT subsamples, respectively. As somewhat expected, we see minor differences between MIUSCAT and
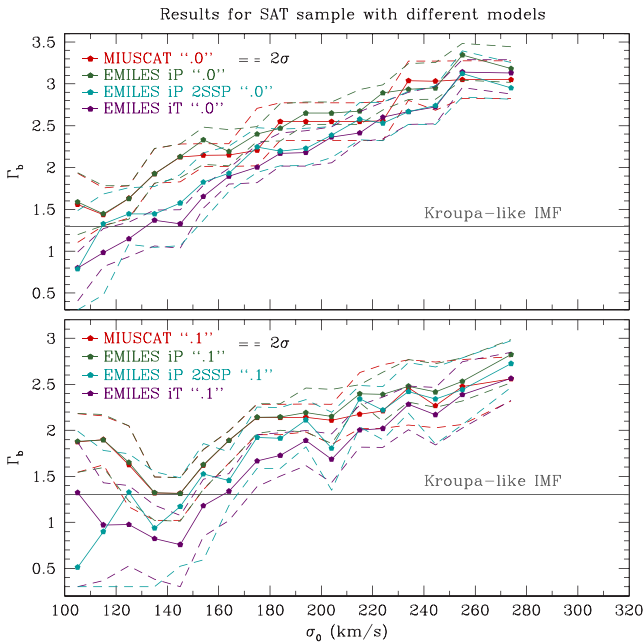
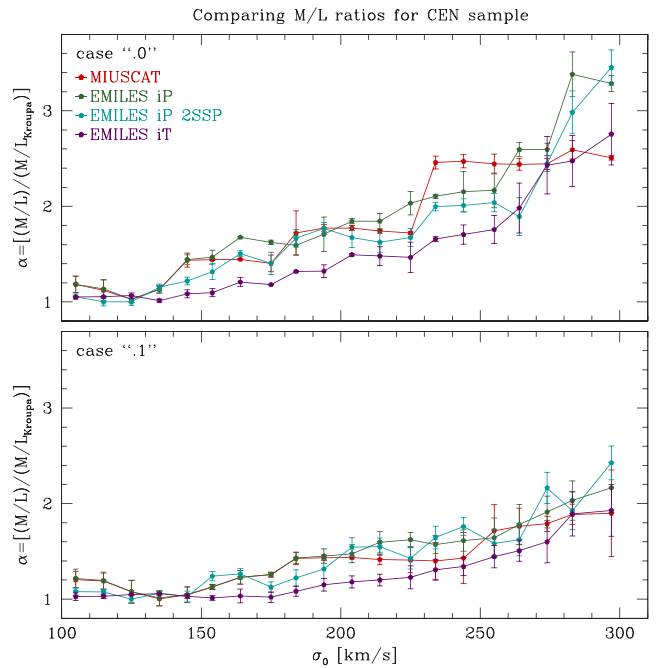**Figure 10.** Same as Fig. 9 but for the subsample of satellites.

Figure 11. Comparison of the M/L obtained from the IMF slopes displayed in Fig. 9 and their corresponding ages and metallicities, for the CEN subsample. Each value of M/L is normalized by the M/L of a stellar population with the same age and metallicity, but with a Kroupa IMF.

EMILES iP models. In fact, these two sets of models coincide in the optical spectral range, but for the fact that EMILES SSPs are provided for a wider range of IMF slopes, Γ_b, with respect to MIUSCAT. Interestingly, both the EMILES iT and EMILES iP 2SSP models yield populations with different ages compared to EMILES iP 1SSP models:

(i) The Teramo models yield older ages with respect to the Padova ones, due to the different temperature scale of the two sets of isochrones (see Vazdekis et al. 2015). This leads to lower values of Γ_b for EMILES iT with respect to EMILES iP, especially for low σ_0 galaxies (see magenta and green curves in Figs 9 and 10). This likely results from the degeneracy between the effects of increasing age and IMF slope on IMF sensitive indices (see e.g. LB13).

(ii) 2SSP models add a small fraction (see LB13) of young stars on top of a predominantly old component. This results into an IMF slope estimate, which is generally lower than for 1SSP models, as seen in Figs 9 and 10 from the offset of the Γ_b–σ_0 relations (cyan relative to green curves). The offset is more pronounced at low σ_0 as the fraction of frosted stars is larger (up to ∼10–15 per cent) for low-mass galaxies, while it becomes less and less important for increasing σ_0.

Finally, we note that, despite differences in the value of Γ_b at fixed σ_0, the general trend of IMF slope becoming more bottom-heavy for increasing σ_0 is well established for all models. Moreover, comparing Fig. 9 and 10 also shows that the Γ_b–σ_0 relation is independent of galaxy hierarchy for all models, i.e. regardless of the adopted set of isochrones, or the assumptions on the galaxy SFH (i.e. the number of SSPs used). The same conclusion holds true also when the M/L of the different samples are compared. Fig. 11 shows this comparison for our central sample CEN, where the M/L ratio shown has been normalized by an M/L ratio calculated with the same age and metallicity, but using a Kroupa IMF (this value is sometimes referred to as the mismatch parameter α in the literature, as we do in the figure). We see that the values of M/L differ slightly from model to model and that the general trend of increasing M/L with σ_0 is recovered in all models. In the calculation of the M/L ratio,

a lower limit of 1.0 has been imposed on Γ_b, because the chosen set of IMF indicators is not sensitive enough to differentiate between a top-heavy and a Kroupa-like IMF. The scatter seen in the figure can be attributed to differences in the models (e.g. different isochrones), while differences in the M/L values among different methods can be attributed to the way abundances, age, and metallicity are estimated from one method to the other.

6 DISCUSSION

6.1 Galaxy central regions and the effect of environment

Our results are obtained for spectra observed within the SDSS fibre diameter, i.e. they refer to the galaxy central regions. In fact, at the median redshift of our galaxy sample, the SDSS fibre has a projected physical radius corresponding to ∼0.5 R_e.

In a two-phase formation scenario (see Section 1), massive ETGs are expected to form their first stars at high redshift during an intense, but short, starburst, and then accrete stars from other smaller systems via galaxy–galaxy interactions (mostly minor mergers and, on average, one major merger, Oser et al. 2012; Naab 2013). Since minor mergers deposit the accreted material in the outskirts of a galaxy, the central regions should contain only stellar populations that have formed at high redshift during the initial starburst. Due to dynamical friction, major mergers are capable of mixing the stellar content of the two galaxies, but since the galaxies have a similar mass, we expect their central parts to have formed on average under similar physical conditions during their initial starburst at high redshift. Hence, it is reasonable to assume, in general, that the light we see in our spectra comes from stars formed in the early stages of galaxy formation.

Various studies observe a correlation between the central velocity dispersion, and thus the stellar mass, and the stellar population properties of ETGs (see Gallazzi et al. 2006; Renzini 2006, and

references therein). The more massive galaxies form their stars in shorter, yet more intense starbursts with respect to their less massive counterparts. More massive galaxies exhibit in this way older, metal richer stellar populations with higher values of [α/Fe].

Environment plays a role in the evolution of galaxies in that it favours or disfavours SF depending on their hierarchy. The SF of satellites is quenched, while the SF of centrals is prolongued. We thus expect to see younger, metal-richer populations with lower [α/Fe] in centrals with respect to satellites at fixed stellar mass (Kuntschner et al. 2002; Pasquali et al. 2009, 2010; de La Rosa et al. 2011; Pasquali 2015).

Finally, we expect the effect of environment to be more pronounced in more massive host haloes, since the resulting gravitational potential is stronger for these objects, the intra-group medium is denser and the halo is more populated.

6.2 Comparison with LB14

The trends of age, metallicity, and [Mg/Fe] with σ_0 of our galaxy sample have been tested against environment. These results are derived in a substantially different way from LB14. We use the line strength of specific indices to derive these stellar population properties, as opposed to the full spectral fitting performed in LB14 (using STARLIGHT; see Cid Fernandes et al. 2005). We additionally allow for the IMF slope to be a free parameter of the fit, as opposed to fixing the IMF at a Kroupa-like value ($\Gamma_b = 1.3$). These two different approaches produce very similar results:

(i) All subsamples have an increasing trend with central velocity dispersion for all properties, except age that flattens above $\sigma_0 = 200 \, \text{km s}^{-1}$.

(ii) Central galaxies show a clear trend with environment, with centrals in high-mass haloes (C2) being younger, more metal-rich, and having lower values of [Mg/Fe] with respect to centrals in low-mass haloes (C1).

(iii) Satellite galaxies in high-mass haloes (S2) show no significant difference to the limit of the given precision in their stellar population properties compared to satellites in low-mass haloes (S1).

We do see however an offset of $+2$ Gyr in age, $+0.1$ dex in metallicity, and -0.05 dex in [Mg/Fe], as described in Section 5.1, between our results and those of LB14. This is most likely due to the different fitting approaches used.

We conclude that the environmental dependence (or lack thereof) of these stellar properties of centrals (satellites) is valid against the two methods employed to analyse the same stacked spectra.

The trend with environment of the properties of centrals can be explained by envisaging that a more massive and thus richer host halo favours a more prolonged star formation history of its central. This would result in younger ages, more metal-rich stars and lower values of [Mg/Fe] in galaxies residing in more massive haloes, since more Type Ia and Type II supernovae were allowed to explode before their SF stopped, enriching the star-forming gas of metals and diluting it with Fe. The lack of trend with host halo mass of satellites can be explained if we consider the quenching of their SF to be mainly an internal process, so independent of environment, or to have occurred on a rather short time-scale (Thomas et al. 2005, 2010; Pasquali et al. 2009, 2010).

We note that centrals and satellites typically reside in haloes of different mass at any given σ_0; thus, their similar trends of stellar population properties and IMF slope as a function of σ_0 should

not be strongly affected by galaxy conformity (cf. for example Weinmann et al. 2006).

6.3 IMF slope

The main result of this work is the lack of dependence of the IMF slope, Γ_b, on galaxy hierarchy and environment. However, we clearly detect a trend towards a more bottom-heavy IMF for ETGs with higher central velocity dispersion. This trend with σ_0 is qualitatively consistent with what was found by previous spectroscopic works (van Dokkum & Conroy 2011; Ferreras et al. 2013; La Barbera et al. 2013, 2016, 2017; Conroy et al. 2013; Spiniello et al. 2014; Martín-Navarro et al. 2015c; van Dokkum et al. 2017; Tang & Worthey 2017), as well as dynamical and lensing studies of massive ETGs (Auger et al. 2010; Treu et al. 2010; Cappellari et al. 2012; Tortora et al. 2013; McDermid et al. 2014; Posacki et al. 2015). The fact that environment does not affect the IMF of ETGs suggests that this property is already established at high redshift, at least for what concerns their central regions. This is consistent with the results of Martín-Navarro et al. (2015b) and Shetty & Cappellari (2014), who found that IMF variations at $z \sim 1$ are similar to those found in nearby ETGs, based on spectroscopy and dynamics, respectively. We argue that the central parts of ETGs have their IMF set at high redshift because, in the current picture of galaxy formation and evolution, these parts form first and because only major mergers are able to mix the central content of two galaxies. Since the masses of two galaxies undergoing a major merger are similar, we expect them to have similar IMF slopes. In addition, major mergers are expected to happen only once on average in the lifetime of a galaxy, so we expect them to be incapable of considerably changing the slope of the IMF in the central parts of an ETG once that slope is set.

This result, especially in the case C1/C2, is in apparent tension with Martín-Navarro et al. (2015c), who found that there is a correlation between the metallicity and the IMF slope in the central regions of massive galaxies. The subsamples C1 and C2 have different metallicities, yet their IMF slope is similar. This apparent conflict with Martín-Navarro et al. (2015c) can be attributed to our stellar population fitting precision and not necessarily to a real inconsistency. If we compare our results for the '.0' and '.1' cases at $\sigma_0 \sim 300 \, \text{km s}^{-1}$, we see a difference in IMF slope of about 0.5, which is significantly larger than the expected IMF difference in the Γ_b–metallicity relation of Martín-Navarro et al. (2015c). In that case, an offset in metallicity of 0.05 dex translates into an IMF slope difference of $\sim$0.15. The difference in IMF slope we observe is, however, comparable with the scatter in the relation, as seen in fig. 2 of their paper. Thus, we conclude that our results are not inconsistent with Martín-Navarro et al. (2015c), but rather suffer from the limitations of the current stellar population fitting precision. Furthermore, the IMF–metallicity relation presented in Martín-Navarro et al. (2015c) refers to systems with high velocity dispersion, so that metallicity alone should not be interpreted as the fundamental driver of IMF variations.

Our analysis takes into account the degeneracy between changes in IMF slope and single elemental abundances. In all three comparisons (C1/C2, S1/S2, CEN/SAT), our '.1' fitting approach – where abundances are fitted to the data directly – shows, in general, a less steep σ_0–IMF relation, and slightly lower values of Γ_b with respect to the '.0' case, where only IMF sensitive features, as well as age and metallicity indicators, are fitted. None the less, both methods predict an IMF more bottom-heavy than Kroupa at the highest σ_0 probed

(∼ 300 km s⁻¹). This result is fully consistent with La Barbera et al. (2015).

We notice here that the two subsamples of centrals divided by halo mass, C1 and C2, do not agree on the value of Γ_b for the lowest σ_0 bins ($\lesssim 150$ km s⁻¹). Since this is the only case where the IMF slope is inconsistent between different subsamples, we have investigated the issue more thoroughly. After running the tests described below (Section 6.3.1), we have concluded that the discrepancy in Γ_b at low σ_0 is likely spurious, and due to a combination of three different factors: (1) some degeneracy between IMF slope and SFH, (2) the lower S/N of the C2 spectra (with respect to C1), and (3) some contamination of the spectra by telluric absorption.

Additionally, we do not expect our definition of environment to significantly alter our results on Γ_b. LB14 has shown that centrals in haloes with $M_h < 10^{12.5}$ M$_\odot$ h^{-1} (our C1 subsample) are mostly isolated (thus representative of very low density environments), while satellites in haloes with $M_h \geq 10^{14}$ M$_\odot$ h^{-1} (S2 subsample) probe by construction high-density regions. If Figs 4 and 6 are compared, no significant variation has been found when comparing C1 and S2 (see also the comparison between CEN and SAT in Fig. 8). This thus implies that our results likely apply also when using other environment indicators.

Finally, we point out that while the central regions of ETGs might indeed not be influenced by the environment where galaxies live in, as shown in this work, their outskirts most likely are. Martín-Navarro et al. (2015a), La Barbera et al. (2016), and van Dokkum et al. (2017) have found that the IMF slope of massive elliptical galaxies shows a radial gradient (but see also Alton et al. 2017), varying from bottom-heavy in the centre to Kroupa-like in the outskirts, beyond a few tenths of R_e. Therefore, it would be interesting, with the aid of ongoing integral field unit spectroscopic surveys (e.g. MaNGa, Bundy et al. 2015), to test if and how IMF radial gradients depend on environment.

6.3.1 IMF slope of centrals at low σ_0

To investigate the origin of the discrepancy between Γ_b for the lowest σ_0 bins of subsamples C1 and C2, we focus on bins having comparable median velocity dispersion between the two subsamples and a significant discrepancy in IMF slope (i.e. 120–130 and 130–140 km s⁻¹ for C1, 100–130 and 130–140 km s⁻¹ for C2), as well as the first bin with good agreement between the two subsamples, taken as a reference bin (140–150 km s⁻¹). We performed different tests, to see if one can leave unchanged the agreement in the reference bin, while making the other σ_0 bins more consistent with each other. The results of the tests can be summarized as follows:

(i) Assuming complex SF histories (EMILES iP with 2SSP models) improves the agreement between the two subsamples. In fact, the sensitivity of spectral indices to variations in IMF slope decreases for lower Γ_b, i.e. for lower σ_0, while their sensitivity to age, metallicity, and abudance ratios remains significant (see La Barbera et al. 2013, specifically the grids in their fig. 11). So, when taking a complex SFH into account (2SSP models) and fitting only IMF sensitive indices ('.0' case), the discrepancy between C1 and C2 is resolved, but when we fit the abundance ratios as well ('.1' case), the difference remains almost unchanged. Additionally, the 2σ contours show a high uncertainty in the values of IMF slope for the '.1' case (see light and dark green points in Fig. 12). It is only because of the large uncertainties that the two subsamples ultimately agree.

(ii) As shown in Fig. A16 of Appendix A, the behaviour of the NaI8190 index – one of the main features used to constrain the
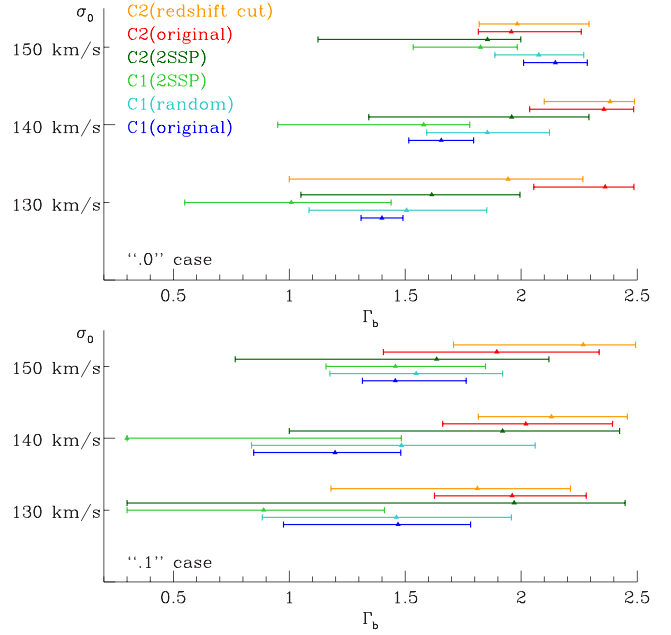

Figure 12. Results of the tests performed to analyse the disagreement of IMF slope values for the three lowest σ_0 stacked spectra of C1 and C2. The bins, which are labelled by the upper limit of their velocity dispersion range, have a similar median velocity dispersion for both C1 and C2. We plot the values of IMF slope (points) with 2σ errorbars. The red and blue symbols are our original results, while the orange and cyan symbols mark, respectively, the values for which C2 has been re-stacked after excluding galaxies with redshift $z \geq 0.082$ (see text), and the values for which C1 has been randomly reduced (in 500 different iterations) to match the number of galaxies of the C2 bins. Cyan symbols give the mean IMF slope, with 2σ confidence intervals, from the 500 iterations. The light and dark green values are those obtained with EMILES iP 2SSP models, used to test the possible degeneracy between IMF slope and SFH. Both the '.0' (upper panel) and the '.1' cases (lower panel) are shown.
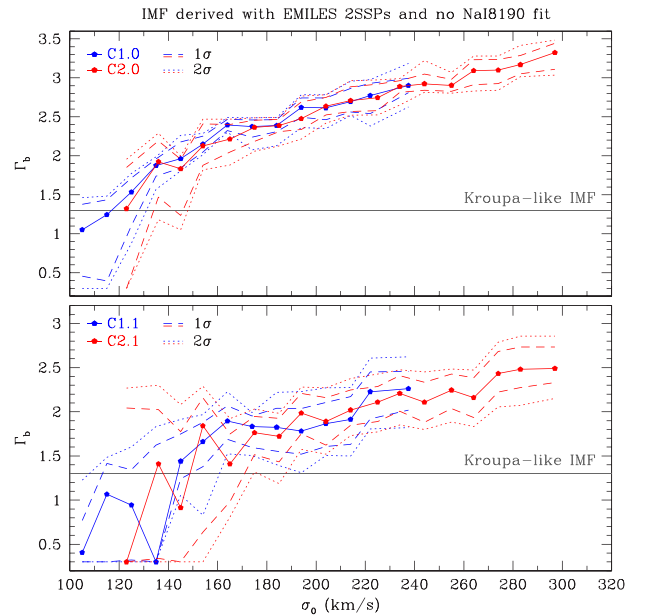

Figure 13. IMF slope-σ_0 trend for C1 and C2 subsamples when 2SSP EMILES models with Padova isochrones are adopted and the NaI8190 index is excluded from the fit. Here, the difference in behaviour for C1 and C2 disappears for both fitting cases ('.0' and '.1').
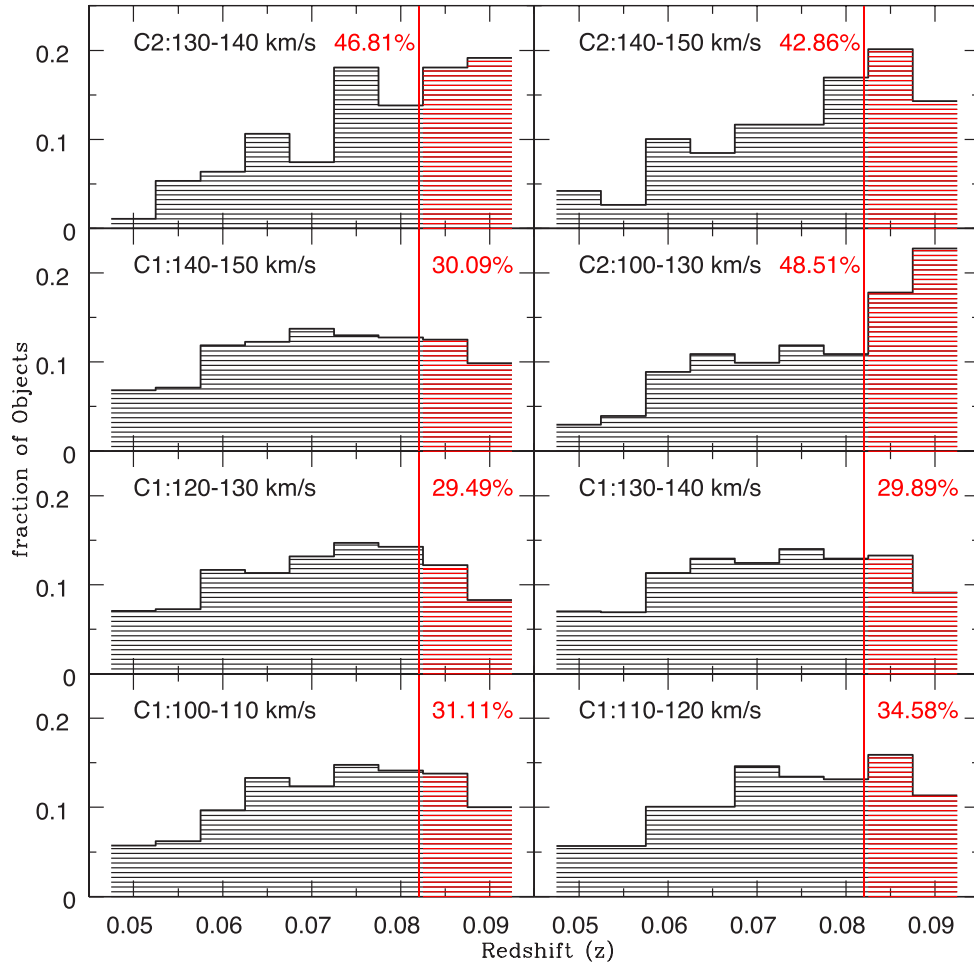
Figure 14. Redshift distribution for the σ_0 bins where C1 and C2 have inconsistent values of Γ_b. The vertical solid line represents the 'critical redshift' at which telluric absorption lines enter the red pseudo-continuum of the NaI8190 index. The red percentages refer to the number of galaxies which have a redshift higher than the critical redshift, and for which telluric absorption might be a concern.

IMF slope – in the lowest σ_0-bins for the C1 and C2 subsamples is very similar to that shown by Γ_b, i.e. the observed line-strengths of NaI8190 are inconsistent between C1 and C2. In fact, if we entirely remove NaI8190 from the fit, C1 and C2 agree in even the lowest σ_0-bins in the '.1' case, while maintaining the same disagreement in the '.0' case. This is the opposite of what happens in the 2SSP test and suggests that the disagreement between C1 and C2 in the lowest σ_0 bins is caused by a combination of a more complex SFH (which is, in fact, expected for low-mass ETGs), and whatever might be affecting the strength of NaI8190. Indeed, Fig. 13 shows that adopting 2SSP models and excluding NaI8190 produces fully consistent results (although with large error bars) between C1 and C2, for both fitting approaches.

(iii) Since the NaI8190 index seems to be partly the reason why Γ_b does not agree between C1 and C2 at low σ_0, we tested if contamination by telluric absorption in the spectra might be responsible for the observed discrepancy. Fig. 14 shows the redshift distribution in the σ_0 bins under study, marking in red the redshift range where telluric contamination can possibly affect the red pseudo-continuum of the NaI8190 index ($z \gtrsim 0.082$). Hence, we construct new C2 stacks by excluding all galaxies at $z > 0.082$. The orange points in Fig. 12 show the results. We see an overall better agreement between C1 and C2 in the 130 km s^{-1} bin in both '.0' and '.1', a slightly larger

difference for the reference bin (140–150 km s^{-1}) in the '.1' case, and still a disagreement in the 130–140 km s^{-1} bin for both fitting cases. Hence, telluric contamination can only explain, in part, the disagreement between C1 and C2.

(iv) Subsample C1 has a significantly larger number of objects in the four σ_0 bins from 100 to 140 km s^{-1} ($N_{C1} = 4532$), resulting into a higher S/N of the stacked spectra, with respect to the two bins (100–130 and 130–140 km s^{-1}) for the C2 subsample ($N_{C2} = 195$). We test the impact of S/N and subsample size on the estimation of IMF slope by randomly reducing the C1 subsample so as to match both the number of galaxies and the σ_0 range of the C2 bins. This 'random' resampling is performed 500 times to obtain a significant statistics of possible outcomes. As shown in Fig. 12, the results of this test (cyan points) imply an overall better agreement with the original C2 values (red points) in the '.1' case. For the '.0' case, the 130 km s^{-1} bin shows only a slightly better agreement, while the other two bins are fully consistent with C2. It is interesting to notice that in contrast to what happens for (iii), it is the 130 km s^{-1} bin that does not change much from its original value, while the 130–140 km s^{-1} bin shifts to values consistent with C2.

In summary, we conclude that the reason why C1 and C2 do not agree in their values of IMF slope in the lowest σ_0 bins is

likely spurious, and results from a complex combination of different effects. To definitively solve the issue, we would need a larger subsample of C2 galaxies with a redshift distribution similar to that of C1.

7 CONCLUSIONS

We select our galaxy sample by cross-matching the SPIDER bona-fide ETGs catalogue of La Barbera et al. (2014) to the group catalogue of Wang et al. (2014), which provides galaxy hierarchy and the mass of the DM host halo assigned to the group the galaxy belongs to. Our final sample consists of 20 996 ETGs with SDSS 1D spectra available. We stack the spectra in bins of central velocity dispersion after dividing them into subsamples based on their hierarchy and host halo mass. We measure a set of absorption line indices to constrain age, metallicity, [Mg/Fe], and IMF slope, by fitting the equivalent widths of these indices with predictions from state-of-the-art synthetic stellar population models (EMILES).

Our results are presented in Figs 3–8 and can be summarized as follows:

(i) Age,[Z/H], and [Mg/Fe]: The general trend of all subsamples shows an increase of these properties with central velocity dispersion, with the exception of age above $\sigma = 200\,\mathrm{km\,s^{-1}}$, which shows a flat dependence. Centrals in higher mass haloes are typically younger, more metal-rich and having lower values of [Mg/Fe] with respect to centrals residing in lower mass haloes. Satellite galaxies in different host haloes are, on the other hand, not influenced by environment to the limit of our precision: their age, metallicity, and [Mg/Fe] are on average compatible within their respective errors. Independently of host halo mass, centrals appear on average younger than satellites. Differences in metallicity between the two subsamples are borderline significant, while their values of [Mg/Fe] are compatible within their respective errors.

(ii) IMF slope: For all subsamples, the IMF slope follows a clear trend with central velocity dispersion σ_0; the higher the σ_0, the more bottom-heavy the IMF. This trend is robust against a number of ingredients (e.g. the set of isochrones used to construct the stellar population models). Hierarchy and host halo mass do not affect significantly the IMF slope. The disagreement between C1 and C2 at low σ_0 is likely spurious, resulting from a complex combination of different factors (a more complex SFH at low σ_0, lower S/N of the C2 subsample, some contamination by telluric lines in the stacked spectra).

We conclude that, while effects of galaxy environment can be observed in the average behaviour of age, metallicity, and [Mg/Fe], the shaping of the IMF slope in the central parts of ETGs is settled in the early stages of galaxy formation, by processes that are not significantly influenced by environment or hierarchy at present day, such as the complex modes of SF in the central regions of these systems in the early stages of their formation. Our motivation to separate external from internal processes (i.e. processes within host halo and galaxy scale, respectively) should be viewed as a first-order approach to understand the role of the different drivers of IMF variations.

REFERENCES

Alton P. D., Smith R. J., Lucey J. R., 2017, MNRAS, 468, 1594
Auger M. W., Treu T., Bolton A. S., Gavazzi R., Koopmans L. V. E., Marshall P. J., Moustakas L. A., Burles S., 2010, ApJ, 724, 511
Barnabè M., Czoske O., Koopmans L. V. E., Treu T., Bolton A. S., 2011, MNRAS, 415, 2215
Bekki K., 2009, MNRAS, 399, 2221
Bell E. F., McIntosh D. H., Katz N., Weinberg M. D., 2003, ApJS, 149, 289
Bernardi M., 2009, MNRAS, 395, 1491
Bernardi M. et al., 2003, AJ, 125, 1849
Bundy K. et al., 2015, ApJ, 798, 7
Cappellari M. et al., 2012, Nature, 484, 485
Cappellari M. et al., 2013, MNRAS, 432, 1862
Cardelli J. A., Clayton G. C., Mathis J. S., 1989, ApJ, 345, 245
Carter D., Visvanathan N., Pickles A. J., 1986, ApJ, 311, 637
Cenarro A. J., Cardiel N., Gorgas J., Peletier R. F., Vazdekis A., Prada F., 2001, MNRAS, 326, 959
Cenarro A. J., Gorgas J., Vazdekis A., Cardiel N., Peletier R. F., 2003, MNRAS, 339, L12
Cervantes J. L., Vazdekis A., 2009, MNRAS, 392, 691
Chabrier G., 2005, in Corbelli E., Palla F., Zinnecker H., eds, Astrophysics and Space Science Library, Vol. 327, The Initial Mass Function 50 Years Later. Springer, Dordrecht, p. 41
Chabrier G., Hennebelle P., Charlot S., 2014, ApJ, 796, 75
Chang J., Macciò A. V., Kang X., 2013, MNRAS, 431, 3533
Cid Fernandes R., González Delgado R. M., Storchi-Bergmann T., Martins L. P., Schmitt H., 2005, MNRAS, 356, 270
Cohen M., 1978, QJRAS, 19, 177
Conroy C., van Dokkum P., 2012a, ApJ, 747, 69
Conroy C., van Dokkum P. G., 2012b, ApJ, 760, 71
Conroy C., Dutton A. A., Graves G. J., Mendel J. T., van Dokkum P. G., 2013, ApJ, 776, L26
Conroy C., van Dokkum P. G., Villaume A., 2017, ApJ, 837, 166
Cushing M. C., Rayner J. T., Vacca W. D., 2005, ApJ, 623, 1115
Davis T. A., McDermid R. M., 2017, MNRAS, 464, 453
de La Rosa I. G., La Barbera F., Ferreras I., de Carvalho R. R., 2011, MNRAS, 418, L74
De Lucia G., Springel V., White S. D. M., Croton D., Kauffmann G., 2006, MNRAS, 366, 499
De Lucia G., Fontanot F., Hirschmann M., 2017, MNRAS, 466, L88
De Masi C., Matteucci F., Vincenzo F., 2018, MNRAS, 474, 5259
Delisle S., Hardy E., 1992, AJ, 103, 711
Duc P.-A. et al., 2015, MNRAS, 446, 120
Dutton A. A., Mendel J. T., Simard L., 2012, MNRAS, 422, L33
Dutton A. A., Macciò A. V., Mendel J. T., Simard L., 2013, MNRAS, 432, 2496
Faber S. M., 1973, ApJ, 179, 731
Faber S. M., French H. B., 1980, ApJ, 235, 405
Falcón-Barroso J., Peletier R. F., Vazdekis A., Balcells M., 2003, ApJ, 588, L17
Ferreras I., Saha P., Williams L. L. R., 2005, ApJ, 623, L5
Ferreras I., Saha P., Burles S., 2008, MNRAS, 383, 857
Ferreras I., Saha P., Leier D., Courbin F., Falco E. E., 2010, MNRAS, 409, L30
Ferreras I., La Barbera F., de la Rosa I. G., Vazdekis A., de Carvalho R. R., Falcón-Barroso J., Ricciardelli E., 2013, MNRAS, 429, L15
Ferreras I., La Barbera F., Vazdekis A., 2015a, in Cenarro A. J., Figueras F., Hernández-Monteagudo C., Trujillo Bueno J., Valdivielso L., eds, Proceedings of the XI Scientific Meeting of the Spanish Astronomical Society, Highlights of Spanish Astrophysics VIII. p. 102

Ferreras I., Weidner C., Vazdekis A., La Barbera F., 2015b, MNRAS, 448, L82

Fontanot F., De Lucia G., Hirschmann M., Bruzual G., Charlot S., Zibetti S., 2017, MNRAS, 464, 3812

Gallazzi A., Charlot S., Brinchmann J., White S. D. M., 2006, MNRAS, 370, 1106

Girardi L., Bressan A., Bertelli G., Chiosi C., 2000, A&AS, 141, 371

Graves G. J., Faber S. M., Schiavon R. P., 2009a, ApJ, 693, 486

Graves G. J., Faber S. M., Schiavon R. P., 2009b, ApJ, 698, 1590

Greene J. E., Janish R., Ma C.-P., McConnell N. J., Blakeslee J. P., Thomas J., Murphy J. D., 2015, ApJ, 807, 11

Gregg M. D. et al., 2006, in Koekemoer A. M., Goudfrooij P., Dressel L. L., eds, Proceedings of a Workshop: The 2005 HST Calibration Workshop: Hubble After the Transition to Two-Gyro Mode. Space Telescope Science Institute, Baltimore, Maryland, p. 209

Gunawardhana M. L. P. et al., 2011, MNRAS, 415, 1647

Gunn J. E., Gott J. R., III, 1972, ApJ, 176, 1

Hardy E., Couture J., 1988, ApJ, 325, L29

Hopkins P. F., 2013, MNRAS, 433, 170

Huang S., Ho L. C., Peng C. Y., Li Z.-Y., Barth A. J., 2016, ApJ, 821, 114

Kapferer W., Sluka C., Schindler S., Ferrari C., Ziegler B., 2009, A&A, 499, 87

Koleva M., Vazdekis A., 2012, A&A, 538, A143

Kroupa P., 2001, MNRAS, 322, 231

Kuntschner H., 2000, MNRAS, 315, 184

Kuntschner H., Smith R. J., Colless M., Davies R. L., Kaldare R., Vazdekis A., 2002, MNRAS, 337, 172

Kuntschner H. et al., 2010, MNRAS, 408, 97

La Barbera F., de Carvalho R. R., de La Rosa I. G., Lopes P. A. A., Kohl-Moreira J. L., Capelato H. V., 2010, MNRAS, 408, 1313

La Barbera F., Ferreras I., de Carvalho R. R., Bruzual G., Charlot S., Pasquali A., Merlin E., 2012, MNRAS, 426, 2300

La Barbera F., Ferreras I., Vazdekis A., de la Rosa I. G., de Carvalho R. R., Trevisan M., Falcón-Barroso J., Ricciardelli E., 2013, MNRAS, 433, 3017 (LB13)

La Barbera F., Pasquali A., Ferreras I., Gallazzi A., de Carvalho R. R., de la Rosa I. G., 2014, MNRAS, 445, 1977 (LB13)

La Barbera F., Ferreras I., Vazdekis A., 2015, MNRAS, 449, L137

La Barbera F., Vazdekis A., Ferreras I., Pasquali A., Cappellari M., Martín-Navarro I., Schönebeck F., Falcón-Barroso J., 2016, MNRAS, 457, 1468

La Barbera F., Vazdekis A., Ferreras I., Pasquali A., Allende Prieto C., Röck B., Aguado D. S., Peletier R. F., 2017, MNRAS, 464, 3597

Leier D., Ferreras I., Saha P., Charlot S., Bruzual G., La Barbera F., 2016, MNRAS, 459, 3677

Lyubenova M. et al., 2016, MNRAS, 463, 3220

McDermid R. M. et al., 2014, ApJ, 792, L37

McDermid R. M. et al., 2015, MNRAS, 448, 3484

Martín-Navarro I., Barbera F. L., Vazdekis A., Falcón-Barroso J., Ferreras I., 2015a, MNRAS, 447, 1033

Martín-Navarro I. et al., 2015b, ApJ, 798, L4

Martín-Navarro I. et al., 2015c, ApJ, 806, L31

Mo H., van den Bosch F. C., White S., 2010, Galaxy Formation and Evolution. Cambridge Univ. Press, Cambridge

More S., van den Bosch F. C., Cacciato M., Skibba R., Mo H. J., Yang X., 2011, MNRAS, 410, 210

Morton D. C., 1991, ApJS, 77, 119

Moster B. P., Somerville R. S., Maulbetsch C., van den Bosch F. C., Macciò A. V., Naab T., Oser L., 2010, ApJ, 710, 903

Naab T., 2013, in Thomas D., Pasquali A., Ferreras I., eds, Proc. IAU Symp. Vol. 295, The Intriguing Life of Massive Galaxies. Kluwer, Dordrecht, p. 340

Newman A. B., Smith R. J., Conroy C., Villaume A., van Dokkum P., 2016, ApJ, 845, 157

Oser L., Ostriker J. P., Naab T., Johansson P. H., Burkert A., 2010, ApJ, 725, 2312

Oser L., Naab T., Ostriker J. P., Johansson P. H., 2012, ApJ, 744, 63

Pasquali A., 2015, Astron. Nachr., 336, 505

Pasquali A., van den Bosch F. C., Mo H. J., Yang X., Somerville R., 2009, MNRAS, 394, 38

Pasquali A., Gallazzi A., Fontanot F., van den Bosch F. C., De Lucia G., Mo H. J., Yang X., 2010, MNRAS, 407, 937

Peletier R. F., 1989, PhD thesis, Univ. Groningen, the Netherlands

Pietrinferni A., Cassisi S., Salaris M., Castelli F., 2004, ApJ, 612, 168

Pietrinferni A., Cassisi S., Salaris M., Castelli F., 2006, ApJ, 642, 797

Posacki S., Cappellari M., Treu T., Pellegrini S., Ciotti L., 2015, MNRAS, 446, 493

Rayner J. T., Cushing M. C., Vacca W. D., 2009, ApJS, 185, 289

Renzini A., 2006, ARA&A, 44, 141

Röck B., Vazdekis A., Ricciardelli E., Peletier R. F., Knapen J. H., Falcón-Barroso J., 2016, A&A, 589, A73

Rogers B., Ferreras I., Pasquali A., Bernardi M., Lahav O., Kaviraj S., 2010, MNRAS, 405, 329

Saglia R. P., Maraston C., Thomas D., Bender R., Colless M., 2002, ApJ, 579, L13

Salpeter E. E., 1955, ApJ, 121, 161

Sánchez-Blázquez P. et al., 2006, MNRAS, 371, 703

Schlafly E. F., Finkbeiner D. P., 2011, ApJ, 737, 103

Serven J., Worthey G., Briley M. M., 2005, ApJ, 627, 754

Shetty S., Cappellari M., 2014, ApJ, 786, L10

Smith R. J., Lucey J. R., 2013, MNRAS, 434, 1964

Smith R. J., Lucey J. R., Carter D., 2012, MNRAS, 426, 2994

Smith R. J., Lucey J. R., Conroy C., 2015, MNRAS, 449, 3441

Spiniello C., Trager S. C., Koopmans L. V. E., Chen Y. P., 2012, ApJ, 753, L32

Spiniello C., Trager S., Koopmans L. V. E., Conroy C., 2014, MNRAS, 438, 1483

Spiniello C., Koopmans L. V. E., Trager S. C., Barnabè M., Treu T., Czoske O., Vegetti S., Bolton A., 2015, MNRAS, 452, 2434

Spinrad H., 1962, ApJ, 135, 715

Tang B., Worthey G., 2017, MNRAS, 467, 674

Thomas D., Maraston C., Bender R., 2003, MNRAS, 339, 897

Thomas D., Maraston C., Bender R., Mendes de Oliveira C., 2005, ApJ, 621, 673

Thomas D., Maraston C., Schawinski K., Sarzi M., Silk J., 2010, MNRAS, 404, 1775

Thomas D., Maraston C., Johansson J., 2011a, MNRAS, 412, 2183

Thomas J. et al., 2011b, MNRAS, 415, 545

Tortora C., Romanowsky A. J., Napolitano N. R., 2013, ApJ, 765, 8

Trager S. C., Worthey G., Faber S. M., Burstein D., González J. J., 1998, ApJS, 116, 1

Trager S. C., Faber S. M., Worthey G., González J. J., 2000, AJ, 120, 165

Treu T., Auger M. W., Koopmans L. V. E., Gavazzi R., Marshall P. J., Bolton A. S., 2010, ApJ, 709, 1195

Trujillo I., Ferreras I., de La Rosa I. G., 2011, MNRAS, 415, 3903

Valdes F., Gupta R., Rose J. A., Singh H. P., Bell D. J., 2004, ApJS, 152, 251

van Dokkum P. G., Conroy C., 2010, Nature, 468, 940

van Dokkum P. G., Conroy C., 2011, ApJ, 735, L13

van Dokkum P. G., Conroy C., 2012, ApJ, 760, 70

van Dokkum P., Conroy C., Villaume A., Brodie J., Romanowsky A. J., 2017, ApJ, 841, 68

Vazdekis A., Casuso E., Peletier R. F., Beckman J. E., 1996, ApJS, 106, 307

Vazdekis A., Peletier R. F., Beckman J. E., Casuso E., 1997, ApJS, 111, 203

Vazdekis A., Cenarro A. J., Gorgas J., Cardiel N., Peletier R. F., 2003, MNRAS, 340, 1317

Vazdekis A., Ricciardelli E., Cenarro A. J., Rivero-González J. G., Díaz-García L. A., Falcón-Barroso J., 2012, MNRAS, 424, 157

Vazdekis A. et al., 2015, MNRAS, 449, 1177

Vazdekis A., Koleva M., Ricciardelli E., Röck B., Falcón-Barroso J., 2016, MNRAS, 463, 3409

Villalobos Á., De Lucia G., Borgani S., Murante G., 2012, MNRAS, 424, 2401

Wang L. et al., 2014, MNRAS, 439, 611

Wegner G. A., Corsini E. M., Thomas J., Saglia R. P., Bender R., Pu S. B., 2012, AJ, 144, 78

Weidner C., Ferreras I., Vazdekis A., La Barbera F., 2013, MNRAS, 435, 2274

Weinmann S. M., van den Bosch F. C., Yang X., Mo H. J., 2006, MNRAS, 366, 2

Weiss A., Peletier R. F., Matteucci F., 1995, A&A, 296, 73

Worthey G., Faber S. M., Gonzalez J. J., 1992, ApJ, 398, 69

Yang X., Mo H. J., van den Bosch F. C., Pasquali A., Li C., Barden M., 2007, ApJ, 671, 153

APPENDIX A: TREND OF MEASURED INDICES WITH σ_0

Figs A1–A18 show the trends of different line strengths used in this work as a function of galaxy velocity dispersion, for different subsamples of ETGs. The leading parameters affecting different line indices are summarized in Table 2. Differently from the results shown in this work, where the observed line strengths have been fitted with models smoothed at the nominal σ_0 of each spectrum, the equivalent widths shown here have been corrected to a reference velocity dispersion of $\sigma = 200\,\mathrm{km\,s^{-1}}$, which lies roughly in the middle of our σ_0 range. This correction is done to permit a direct comparison between bins of different velocity dispersion and has been performed in the following manner:

(i) We select five MIUSCAT model spectra, four with a Kroupa-like IMF ($\Gamma_b = 1.3$) and with young (7 Gyr) and old (14 Gyr), as well as solar and super-solar ([Z/H] = 0.22) metallicities. The

Figure A1. Trend of the C4668 line with σ_0 for the stacked spectra of C1/C2, S1/S2 and CEN/SAT, respectively. C4668 is mainly used to fit [C/Fe] in the '.1' case.
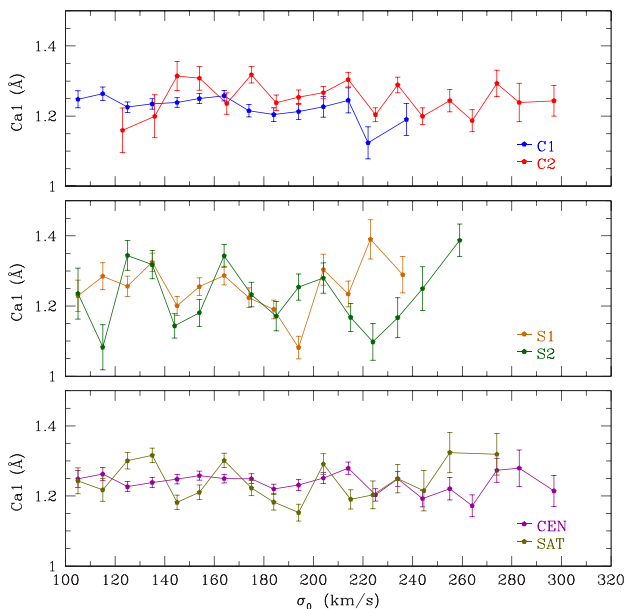
Figure A2. Trend of the Ca1 line with σ_0. Ca1 is mainly used to fit [Ca/Fe], jointly with Ca4227 and CaH&K, in the '.1' case.
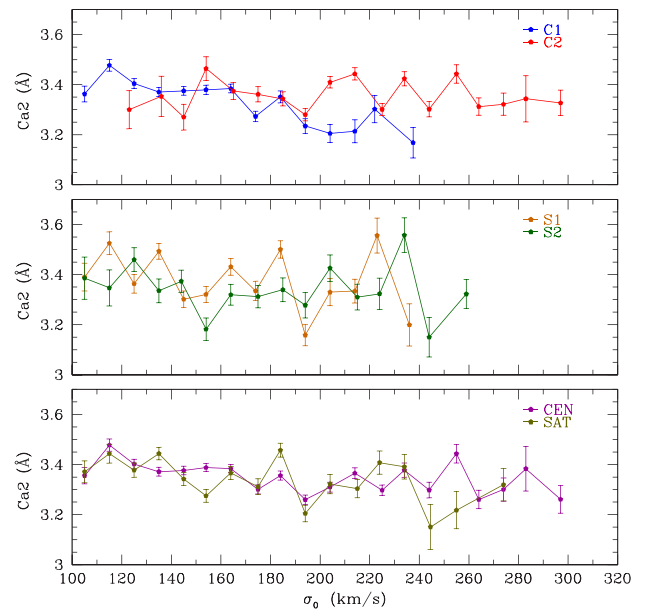
Figure A3. Trend of the Ca2 line with σ_0. Ca2 is mainly used to fit the slope of the IMF.
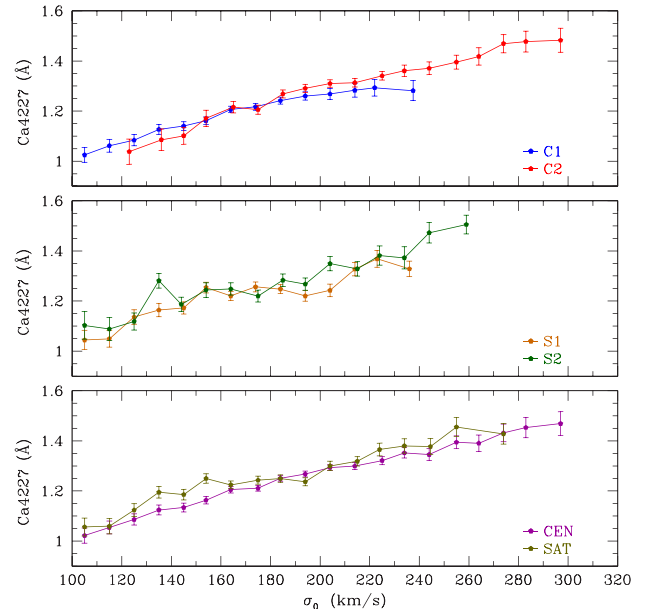
Figure A4. Trend of the Ca4227 line with σ_0. Ca4227 is mainly used to fit [Ca/Fe], jointly with Ca1 and CaH&K, in the '.1' case.
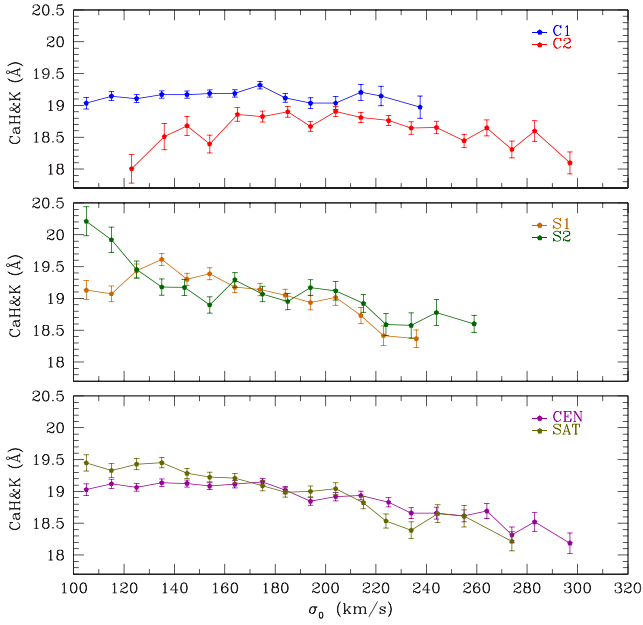
Figure A5. Trend of the CaH&K line with σ_0. CaH&K is mainly used to fit the slope of the IMF and [Ca/Fe], jointly with Ca1 and Ca4227.
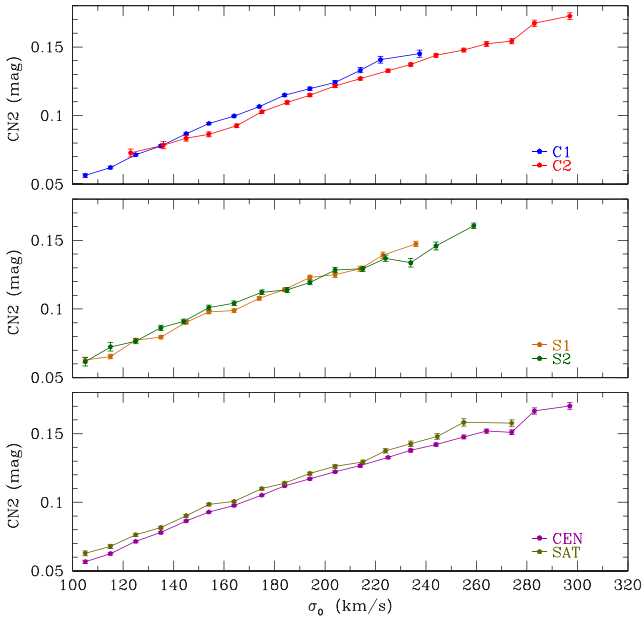

Figure A6. Trend of the CN2 line with σ_0. CN2 is mainly used to fit [N/Fe], [O/Fe] and, jointly with C4668, [C/Fe] in the '.1' case.
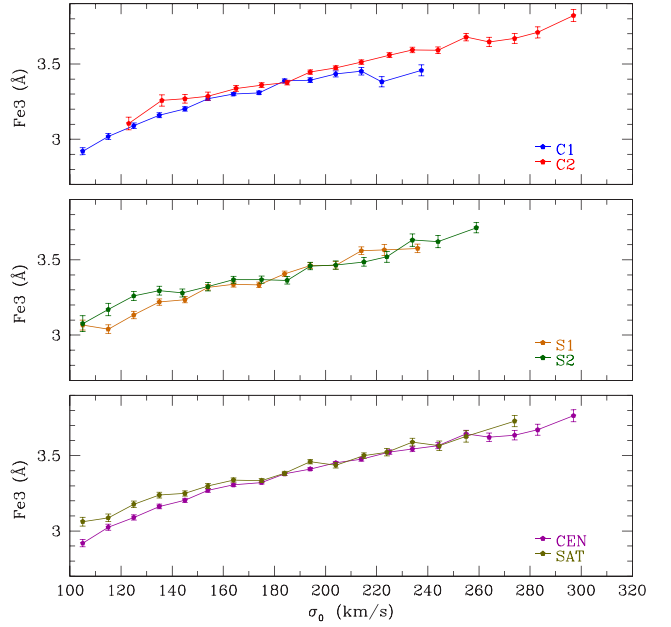

Figure A7. Trend of the Fe3 line with σ_0. Fe3 is mainly used, jointly with Mgb5177, to determine the value of the [α/Fe] proxy of the stacked spectrum.
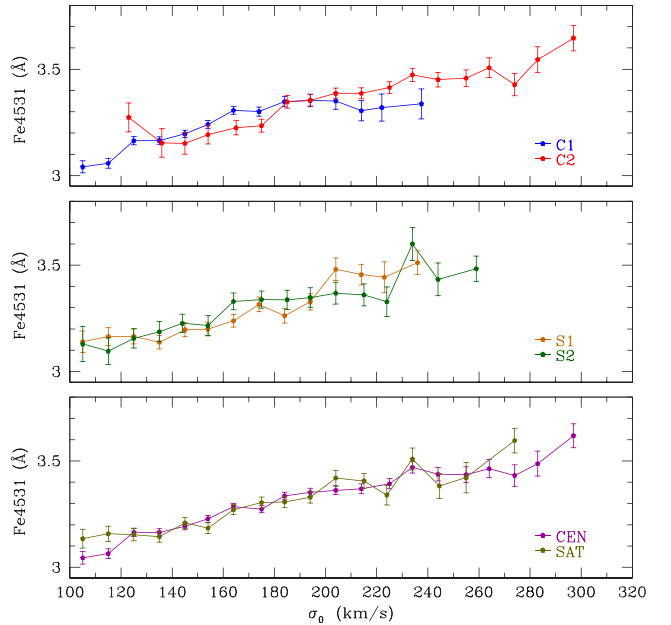

Figure A8. Trend of the Fe4531 index with σ_0. Fe4531 is mainly used to fit [Ti/Fe], jointly with TiO1 and TiO2$_{SDSS}$, in the '.1' case.

fifth model is constructed using a super-solar, old population with a bottom-heavy IMF ($\Gamma_b = 2.8$).

(ii) We choose a velocity dispersion sample $\sigma_i = [100, 320]$ km s^{-1}, with a step of 10 km s^{-1} between σ_i and σ_{i+1}, and use the resulting velocity dispersions to broaden the model spectra described in the point above.

(iii) We then measure the equivalent width of all the indices from our five sets of broadened model spectra.

(iv) The correction of a given index measured from a spectrum with $\sigma_0 = \sigma_i$ is taken as the difference between the equivalent width of the index measured in the model spectrum at $\sigma_i = 200$ km s^{-1} and the equivalent width of the index measured in the model spectrum at

σ_i: $\Delta EW_i = EW_{200,mod} - EW_{\sigma_i,mod}$. Finally, the correction applied to the measured equivalent widths is the median of the five ΔEW_i calculated from each set of model spectra.

We notice that, as expected, the line strengths of all metallic lines increase with central velocity dispersion, with the exception of the Ca lines, which remain almost constant as a function of σ_0. The age sensitive H β_o line decreases with σ_0, consistently with what is shown in Section 5.

Furthermore, small differences are present between different subsamples (in particular C1 and C2) consistent with the results shown
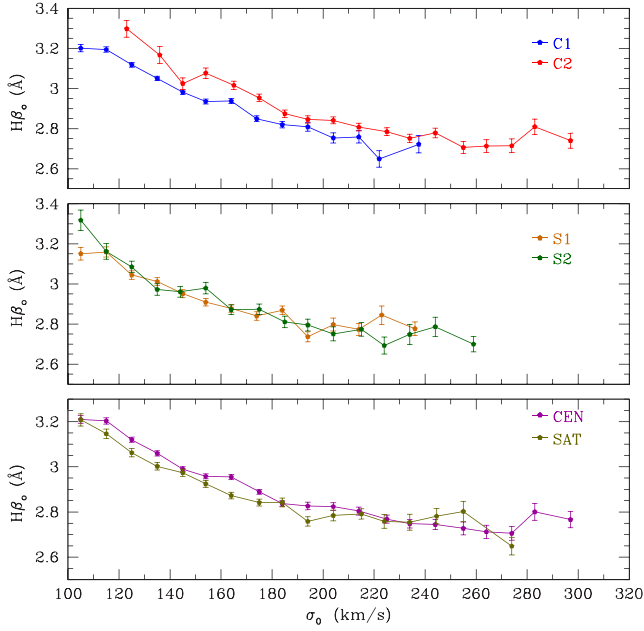
Figure A9. Trend of the Hβ_o line with velocity dispersion σ_0. Hβ_o is mainly used as a proxy for the age of the stellar population of the stacked spectrum. The values of Hβ_o shown are corrected for nebular emission.
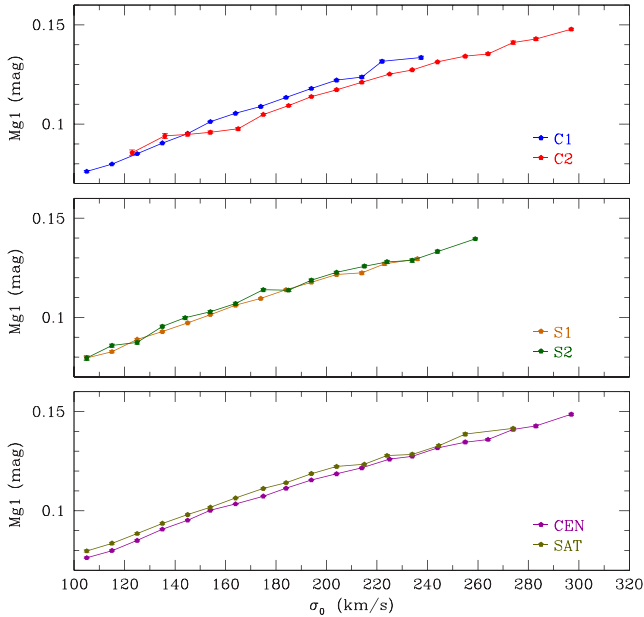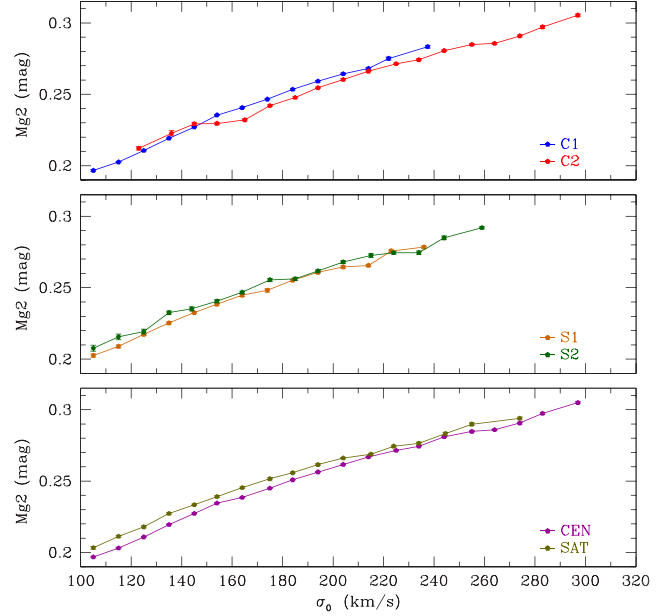

Figure A11. Trend of the Mg2 line with σ_0. Mg2 is mainly used to fit [Mg/Fe] and [Si/Fe] in the '.1' case.

Figure A10. Trend of the Mg1 line with σ_0. Mg1 is mainly used to fit [O, Ne, S/Fe], [C/Fe] and Si/Fe in the '.1' case.
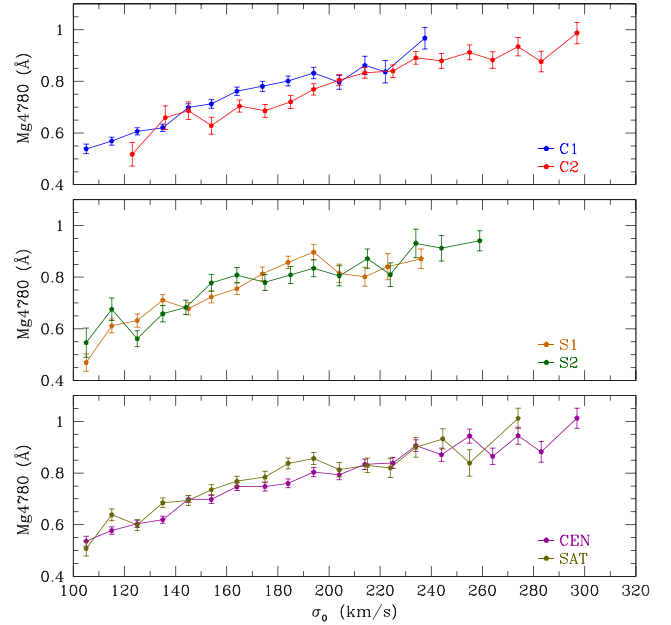
Figure A12. Trend of the Mg4780 line with σ_0. Mg4780 is mainly used to fit the slope of the IMF.

in Section 5.1. For instance, Mgb5177 (Fe3) is lower (higher) for C2 with respect to C1, which is consistent with our result showing that C2 ETGs have slightly lower [Mg/Fe] and higher metallicity than their C1 counterparts.

Finally we also notice, as described in Section 6.3.1, that the index NaI8190 (Fig. A16) shows a very clear separation between C1 and C2 at low σ_0, very similar to what we observed in the behaviour of the IMF slope.
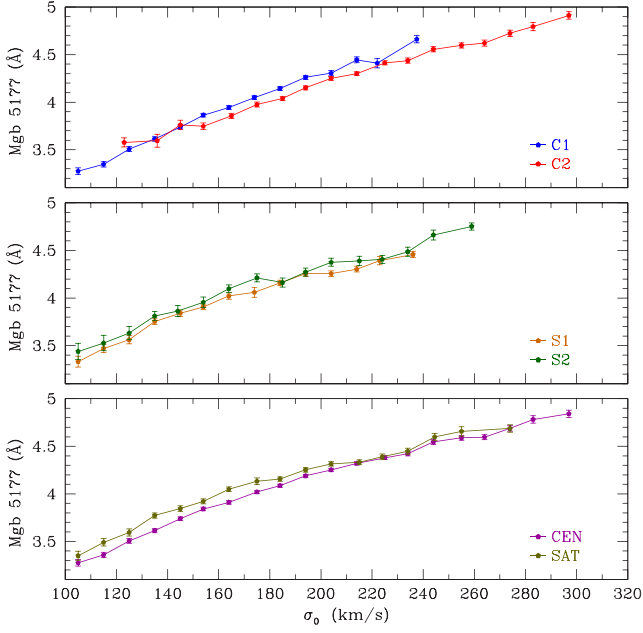
Figure A13. Trend of the Mgb5177 line with σ_0. Mgb5177 is mainly used to compute [MgFe]′, to fit [Mg/Fe] and, jointly with Fe3, to determine the proxy of [α/Fe].
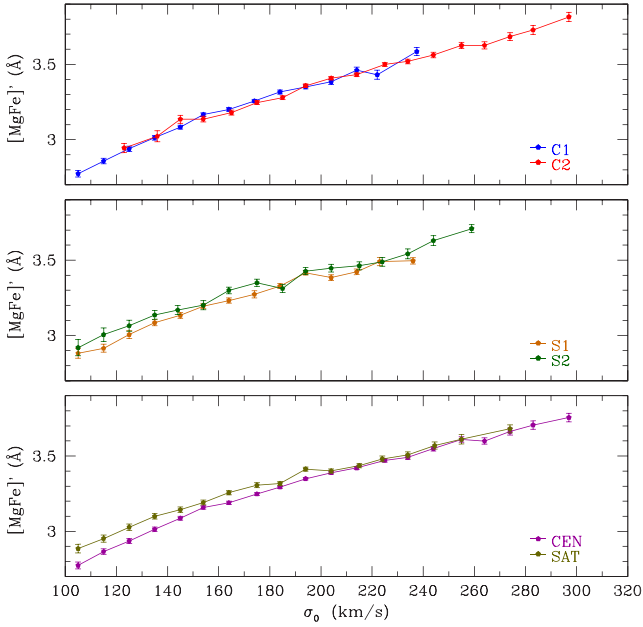

Figure A14. Trend of the [MgFe]′ line with σ_0. [MgFe]′ is mainly used as a proxy for the metallicity of the stacked spectrum.
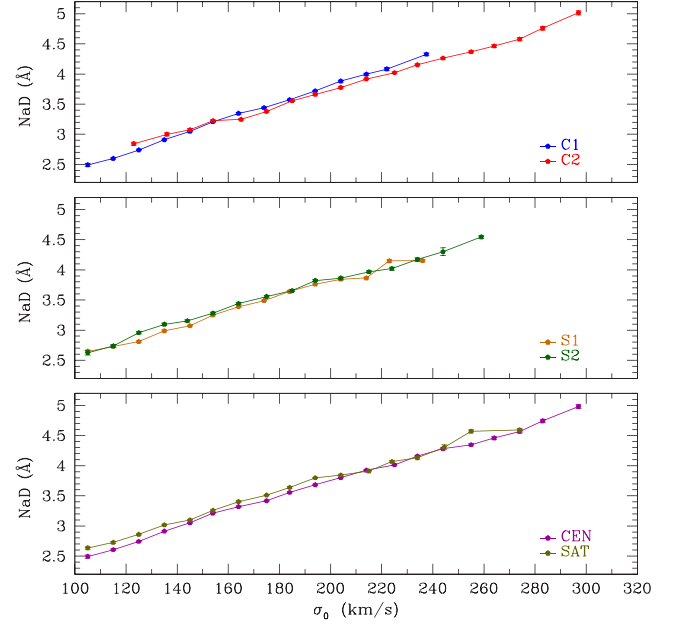

Figure A15. Trend of the NaD line with σ_0. NaD is mainly used to fit the slope of the IMF and to fit [Na/Fe], jointly with NaI8190.
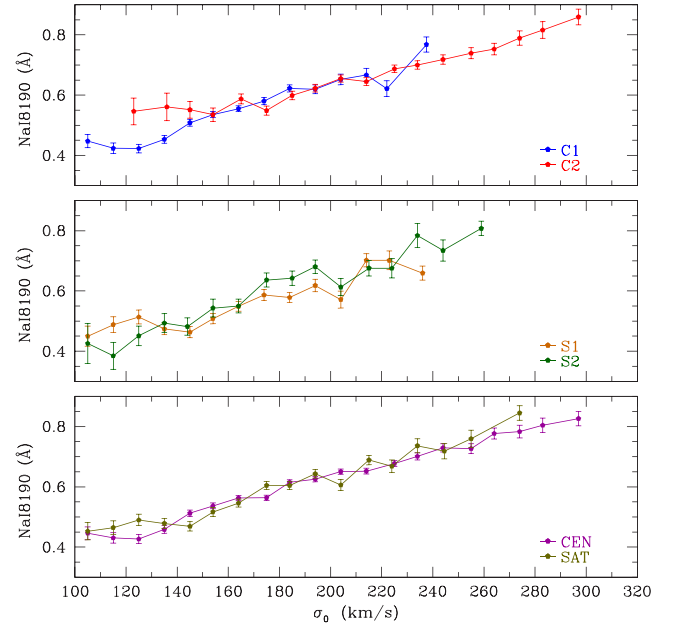

Figure A16. Trend of the NaI8190 line with σ_0. NaI8190 is mainly used to fit the slope of the IMF and [Na/Fe], jointly with NaD.

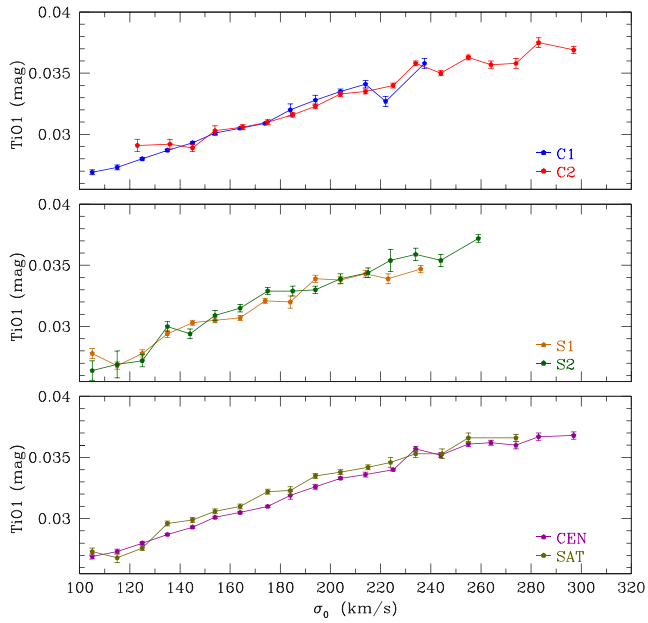**Figure A17.** Trend of the TiO1 line with σ_0. TiO1 is mainly used to fit the slope of the IMF and [Ti/Fe], jointly with TiO2$_{SDSS}$ and Fe4531.
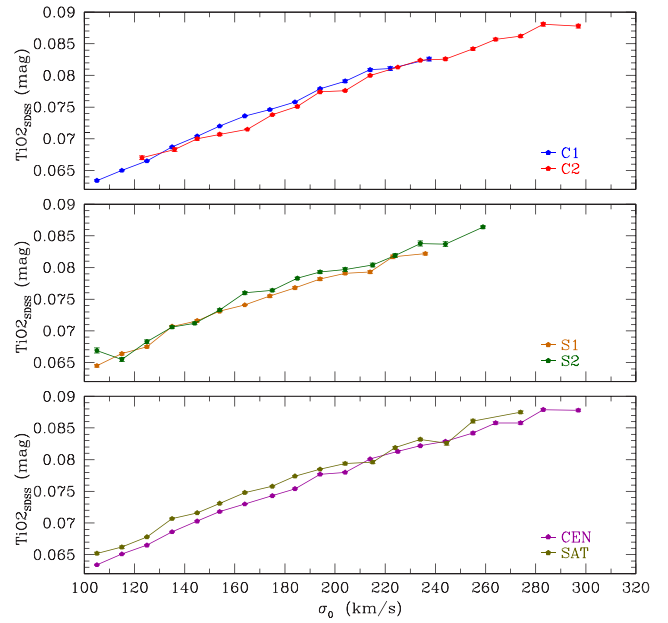

Figure A18. Trend of the TiO2$_{SDSS}$ line with σ_0. TiO2$_{SDSS}$ is mainly used to fit the slope of the IMF and [Ti/Fe], jointly with TiO1 and Fe4531.

This paper has been typeset from a TEX/LATEX file prepared by the author.